Chemical reaction thresholds according to classical-limit quantum dynamics

L. Bonnet, C. Crespos, M. Monnerville

Chemical reaction thresholds according to classical-limit quantum dynamics.

L. Bonnet,[*,†] C. Crespos,[*,†] and M. Monnerville[*,‡]

† *Univ. Bordeaux, CNRS, Bordeaux INP, ISM, UMR 5255, F-33400 Talence, France*

‡ *Univ. Lille, CNRS, PHLAM, UMR 8523, 59655 Villeneuve dAscq, France*

E-mail: claude-laurent.bonnet@u-bordeaux.fr; cedric.crespos@u-bordeaux.fr;

maurice.monnerville@univ-lille.fr

Abstract

Classical-limit quantum dynamics is used to explain the origin of the quantum thresholds of chemical reactions from their classical dynamics when these are vibrationally nonadiabatic across the interaction region. The study is performed within the framework of an elementary model of chemical reaction that mimics the passage from free rotation of the reagents to bending vibration at the transition state to free rotation of the products.

1 Introduction

Threshold energies (or thresholds) of simple barrier reactions play a key role in chemistry because they determine to a large extent, mainly through the exponential term of Eyring's equation, the rate at which these reactions occur (we will focus our developments on bimolecular reactions in the electronic ground state).[1–3] If we define the *transition state* (TS) of a given barrier reaction by the "molecule" whose coordinates are transverse to the reaction path at the barrier top, the threshold energy E_{th} with respect to the potential energy of the reactants in their equilibrium geometry is given to a good approximation by

$$E_{th} = V^{\ddagger} + E^{\ddagger}_{zpe}, \tag{1}$$

where $V^{\ddagger}$ is the classical barrier heigth and $E^{\ddagger}_{zpe}$ is the zero point energy (ZPE) of the transition state (TS-ZPE).[4] Eq. (1) is supported by the fact that the rate constants found by means of transition state theory (TST) are in much better agreement with experimental rate constants when the vibrational motions of the TS are treated quantum mechanically rather than classically.[2,3,5,6] Moreover, quantum dynamical calculations corroborate the validity of this equation.[7–13]

For some reactions, couplings between vibrational motion orthogonal to the reaction path and motion along the reaction path remain negligible across the interaction region slightly

above threshold. The dynamics are then vibrationally adiabatic throughout the process. This is for instance the case of the collinear reaction H+$H_2(v = 0)$ up to ~ 0.2 eV above the threshold.[14] For others, the previous couplings are non negligible and the dynamics are vibrationally nonadiabatic across the interaction region.

For vibrationally adiabatic reactions, one may classically justify Eq. (1) as follows: trajectories start from the reagents in the rovibrational ground-state, of energy E_{zpe}, and with the total energy E, or equivalently, the collision energy $E - E_{zpe}$. If the latter is sufficiently large for the system to climb the barrier, all the trajectories reach the TS with the vibrational energy $E^{\ddagger}_{zpe}$ since the dynamics are vibrationally adiabatic across the interaction region. Thus, the kinetic energy at the TS is equal to $E - V^{\ddagger} - E^{\ddagger}_{zpe}$. Clearly, E_{th} is the value of E that makes the previous kinetic energy zero, which implies Eq. (1). Therefore, the threshold energy is associated with the trapping of trajectories in a metastable or resonant state at the transition state. Finally, the energy dependence of the reaction probability is a Heaviside step function centered at E_{th}. The quantum mechanical justification of Eq. (1) involves similar ideas, except that tunneling through the vibrationally adiabatic ground-state barrier leads to the smearing of the Heaviside step. Note that since the early 70's, the adiabaticity assumption is the basis of many studies involving approximate statistical or quantum dynamical calculations of reaction cross sections or rate constants.[3,11,15–19]

For vibrationally nonadiabatic reactions, it usually happens that some trajectories starting from the reagents with E_{zpe} cross the transition state with a vibrational energy lower than $E^{\ddagger}_{zpe}$. Obviously, these trajectories make the classical threshold lower than $V^{\ddagger}+E^{\ddagger}_{zpe}$.[9,12] Therefore, classical dynamics generally contradicts Eq. (1), unlike quantum dynamics which usually supports it regardless of the nature of the vibrational dynamics. In other words, quantum dynamics appears to be more vibrationally adiabatic than classical dynamics.[9] What are the basic reasons for this difference in behaviour ? Schatz has argued that quantization of the vibrational motion at the barrier top is imposed by the uncertainty principle.[9] Besides, Pollak and co-workers have carried out in-depth studies on adiabaticity-related issues that shed

light on the previous question.[6,10,11,20] The aim of the present work is to complement these studies with an alternative analysis of the physics underlying Eq. (1) within the framework of the classical-limit quantum dynamical approaches pioneered by Miller and Marcus.[21–25] Classical-limit quantum dynamics, more often called semiclassical dynamics, assigns probability amplitudes to classical paths and make them interfere according to the superposition principle. Regarding reaction thresholds, one expects that interferences will be destructive below the threshold given by Eq. (1), constructive above. The first goal of this work is to demonstrate the validity of this scenario within a simple model of vibrationally nonadiabatic reaction, and we will use both the semiclassical initial value representation[22,26,27] (SCIVR) and classical S-matrix theory[21,22,24,25,28] (CSMT) to achieve it.

A realistic semiclassical treatment of the dynamics around the threshold should take into account tunneling through classically prohibited area of the potential energy barrier (dynamically or energetically). For CSMT and the type of SCIVR approach that we will be using in the following,[22,27] the most rigorous way to achieve this would require running trajectories in complex time rather than in real time.[29–31] However, this would make the study more involved, both technically and conceptually (technically because complex time trajectories are difficult to calculate, and conceptually since disentangling tunneling from the TS-ZPE effect is likely to be nontrivial). For simplicity's sake, we will thus consider a model potential energy surface (PES) with no potential energy barrier along the reaction path ($V^{\ddagger} = 0$), so E_{th} will be equal to $E^{\ddagger}_{zpe}$ [see Eq. (1)].[12] Therefore, tunneling will be strongly minimized and real-time classical paths sufficient for a relatively accurate description of the reaction dynamics. This will allow us to focus our efforts on the TS-ZPE effect alone, which is ideal for better understanding its causes. We will still have the possibility, in the future, to study how the addition of a potential energy barrier modifies the conclusions obtained in the present work.

Three decades ago, Friedman and Truhlar showed that reaction thresholds are associated with poles of the S-matrix, well known to define quantum scattering resonances.[32] Therefore,

they proved that reaction thresholds are intimately related to resonances, as shown previously within the classical picture in the vibrationally adiabatic case. Yet, if this definition in terms of poles has the merit of rigor, it remains quite abstract. In comparison, the classic definition of a resonance as an effect resulting from phase-matching is intuitively more appealing. A standard illustration of this definition is that of soldiers marching in step on a bridge; if the frequency of marching is equal to the natural frequency of the bridge, the latter can collapse if it is not strong enough. (This was the case of the Broughton suspension bridge on April 12, 1831.) It is this type of resonant phase-matching that one might wish to highlight in the theoretical description of chemical reactions in order to explain in simple terms the origin of thresholds for vibrationally nonadiabatic reactions. We will see later on that this goal, the second of this work, can also be achieved within the framework of the semiclassical treatment of our model reaction. In fact, both goals converge and they will be reached at the same time.

The paper is organized as follows. The model of vibrationally nonadiabatic reaction is defined in Sec. 2. The energy dependence of the reaction probability obtained from quantum mechanical calculations is compared with those resulting from classical trajectory and SCIVR calculations in Sec. 3. SCIVR reproduces the sigmoidal shape of the quantum threshold which is nearly centered at $V^{\ddagger} + E^{\ddagger}_{zpe}$, whereas the classical threshold coincides with $V^{\ddagger}$ (here taken at 0). In Sec. 4, these findings are analysed within CSMT. Intuitively appealing analytical expressions are derived that enable to explain the quantum threshold from the properties of relevant classical paths and the superposition principle. Sec. 5 concludes.

2 Model reaction

For a chemical reaction involving a potential energy barrier, the PES "felt" by the system in the neighborhood of the saddle point is well approximated by its second order expansion. The PES around the saddle point is then given by the sum of an inverted parabola along

the reaction path, and a parabola along the coordinate orthogonal to the reaction path. Consequently, the vibrational dynamics are adiabatic in the vicinity of the TS, located at the barrier top.[33] On the other hand, strong couplings between the two previous degrees-of-freedom are in general present on way from the reagents to the TS, and on way from the TS to the products. Slightly above threshold, the internal state along the coordinate orthogonal to the reaction path is thus perturbed on the climb to the TS, unperturbed around the TS, and perturbed again on the descent to the product valley (or back to the reagent valley). Such dynamics are well summarized by the expression state-to-state-to-state dynamics.[34] Below, we propose a simple model of barrierless reaction involving this type of dynamics.

We consider a fixed-plane of the laboratory and a rigid diatom rotating within this plane. Moreover, we force the center-of-mass of the diatom to move on a given R-axis of the plane. The orientation of the diatom with respect to R is determined by the angle ϕ. Our model PES is given by:

$$V(R,\phi) = \frac{\alpha sin^2(\phi/2)}{cosh(2\beta R) + cosh(\beta\Delta)} \tag{2}$$

with $\alpha = 4.053$ eV, $\Delta = 2$ Å and $\beta = 3$ Å^{-1}. (A similar potential was proposed in Ref.[12] by G. Schatz.) This PES, represented in Fig. 1, involves a narrow channel separating the reagent and product planes. An example of reactive trajectory starting from the reagent plane with no rotational excitation is represented by the yellow line. In the numerical calculations, we will indeed assume that the initial diatom is in the rotational ground-state $j_1 = 0$. The trajectory goes from $(R_1 = -3\ \mathring{A}, \phi_1)$ to $(R_2 = 3\ \mathring{A}, \phi_2)$. Miller's *shifted angles* $(\overline{\phi}_1, \overline{\phi}_2)$, involved in next developments (see Sec. 3.1.3), are also shown. Within the interaction region, there is only one periodic orbit (PO), trapped along the ϕ-axis. This orbit is represented in Fig. 1 by a turquoise segment (the yellow and turquoise orbits are both at the same energy). Pechukas and Pollak showed that the TS is the phase space surface whose projection on the (R, ϕ) configuration plane coincides with the representation of the PO in the same plane.[35,36] The TS is thus trivially defined here by $R = 0$. The reactive trajectory clearly mimics the passage from free rotation of the reagents to bending vibration at the

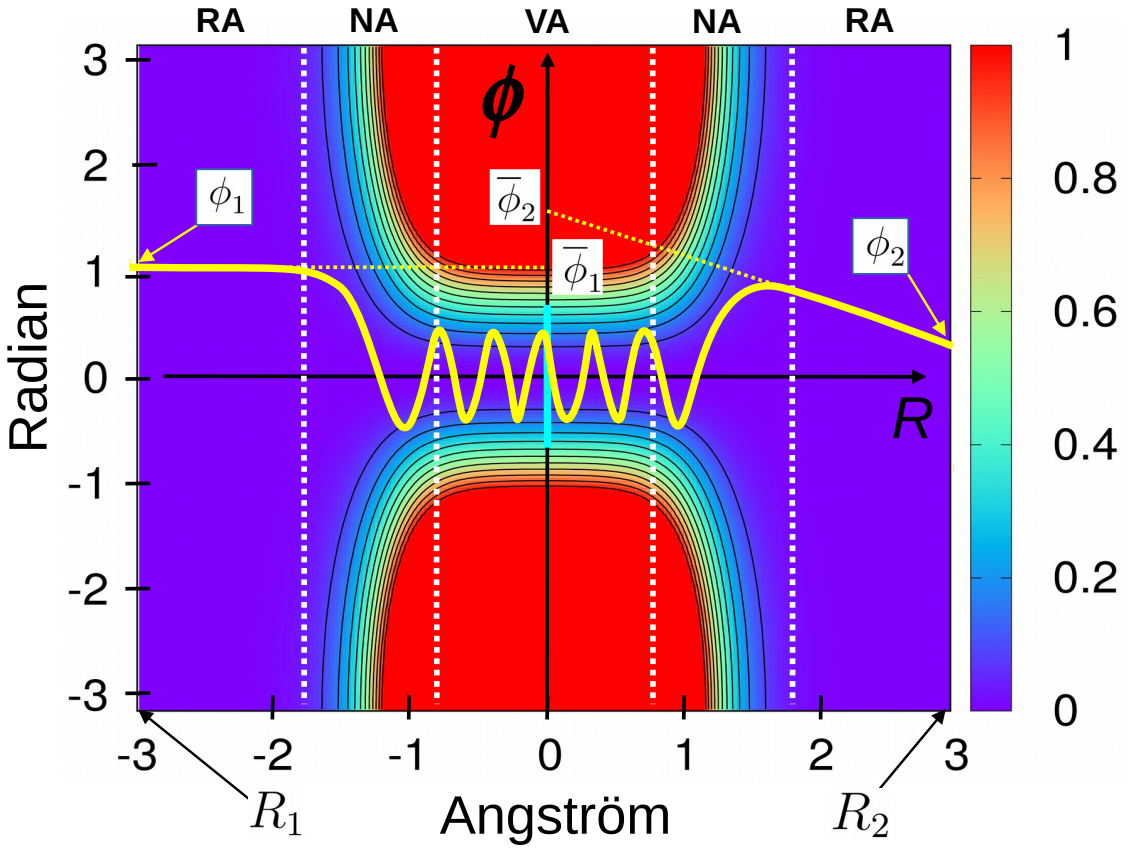

Figure 1: Model PES used in this work. The reagent and product (half) planes, respectively on the left and on the right of the outermost white dashed lines, are separated by a channel. Along the R-axis, which represents the reaction path, the potential is 0. Note that ϕ runs from $-\pi$ to π. An example of reactive trajectory starting from the reagent plane with no rotational excitation (yellow curve) as well as the only periodic orbit trapped within the interaction region (turquoise segment) are shown. This periodic orbit defines the TS of the reaction. The yellow path is run from (R_1, ϕ_1) to (R_2, ϕ_2), with $R_2 = -R_1 = 3$ Å. The four white vertical dashed lines define three bands between the side plains. The dynamics are rotationally adiabatic (RA) within the plains, vibrationally adiabatic (VA) within the central band, and nonadiabatic (NA) in the two remaing bands where the R and ϕ coordinates are strongly coupled. The yellow dashed lines show the geometrical relation between the so-called shifted angles $(\overline{\phi}_1, \overline{\phi}_2)$, useful in the following, and the angles (ϕ_1, ϕ_2).

transition state to free rotation of the products that occurs in realistic bimolecular reactions. Four white vertical dashed lines define five regions labeled RA, NA or VA above the frame of Fig. 1. The dynamics are rotationally adiabatic in the RA reagent and product half planes, vibrationally adiabatic in the VA central region encompassing the TS, and nonadiabatic in

the NA regions due to the presence of strong couplings between the R and ϕ coordinates.

We will call *activated complex* the system orthogonal to the reaction path in the VA region. Within this definition, the activated complex coincides with the TS at $R = 0$. Besides, the activated complex has a lifetime, contrary to the TS which is just crossed by classical trajectories.

The classical Hamiltonian of the system is

$$H = \frac{P^2}{2\mu} + \frac{J^2}{2I} + V(R, \phi) \tag{3}$$

where $P = \mu \frac{dR}{dt} = \mu \dot{R}$ and $J = I \frac{d\phi}{dt} = I \dot{\phi}$ are the momenta conjugate to R and ϕ, respectively, μ is the mass associated with motion along the R-axis, and I is the moment of inertia of the diatom, taken at 0.2768 g.mol^{-1} Å^2. From the second order development $\frac{1}{2} I {\omega^{\ddagger}}^2 \phi^2$ of $V(R, \phi)$ along the ϕ-axis, $E^{\ddagger}_{zpe}$, approximately given by $\frac{\hbar \omega^{\ddagger}}{2}$, is found equal to 705 cm^{-1}. This value typically corresponds to that for a bending vibration. (Since the range of available angles at 705 cm^{-1} is much narrower than 2π, the previous harmonic approximation is quite realistic.) Two values of μ will be considered, 19 amu and 1.9 amu. The parameters are set so that our model process roughly mimics a triatomic heavy plus heavy-light reaction for $\mu = 19$, and a light plus heavy-light reaction for $\mu = 1.9$. The total energy E of the reaction will be limited to the range $[0.8 E^{\ddagger}_{zpe}, 1.2 E^{\ddagger}_{zpe}]$ for $\mu = 19$ and $[0.6 E^{\ddagger}_{zpe}, 1.4 E^{\ddagger}_{zpe}]$ for $\mu = 1.9$. All actions will be expressed in $\hbar$ unit, except in Sec. 4.2.

Finally, one should note that the absence of a potential energy barrier on the PES does not preclude the presence of a barrier of 705 cm^{-1} on the vibrationally adiabatic ground-state curve. It is only in this sense that our model reaction brings into play a barrier.

3 Energy dependence of the reaction probability

3.1 Theoretical approaches

3.1.1 Quantum method

The quantum calculations have been performed by using the standard Time Dependent Wave Packet (TDWP) approach in which a wave packet (WP) initialy located in the reagent plane is propagated up to the products where it is finally analyzed.[37] In these calculations, the time propagation is achieved using the split-operator method[38,39] with the propagation time t being discretized with uniform time steps Δt. The initial state describing the system is built as the direct product :

$$\psi_{j_1}(R, \phi, t = 0) = G(R)\, \varphi_{j_1}(\phi) \tag{4}$$

where

$$G\,(R) = \left(\frac{1}{2\pi\sigma^2}\right)^{\frac{1}{4}} \exp\left[-\frac{(R - R_0)^2}{4\sigma^2} + ik_0(R - R_0)\right] \tag{5}$$

is an incoming Gaussian WP (GWP) centered at R_0, with a width σ and a mean kinetic energy $\langle E_0 \rangle = (1/2\mu)\,[k_0^2 + 1/4\sigma^2]$, and where

$$\varphi_{j_1}(\phi) = \frac{1}{\sqrt{2\pi}} e^{ij_1\phi} \tag{6}$$

is the plane wave corresponding to the initial rotational state j_1 (for generality's sake, we present all the theoretical formulations for any value of j_1 though we will only apply them to the case $j_1 = 0$ in the following). $\psi_{j_1}(R, \phi, t = 0)$ is travelling from left to right, i.e., R_0 is negative and k_0 is positive. The action of the Hamiltonian $\hat{H}$ onto the wave packet is computed using local representations of each operator, namely, a discrete variable representation[40–42] (DVR) for the potential energy operator, and a finite basis representation (FBR) for the radial and angular kinetic energy operators. The DVR is based on a direct product

grid of $N_R \times N_\phi$ points, corresponding to equally spaced grid points for both the radial R and angular ϕ coordinates. The basis set of the related FBR is defined as a direct product of $N_R \times N_\phi$ plane waves. The kinetic energy terms are calculated in the FBR while the potential one is determined in the DVR. The transformations DVR $\leftrightarrow$ FBR are performed by a two-dimensional fast Fourier transform.[43] Complex absorbing potentials (CAPs) are employed to avoid unphysical reflections of the wave packet at the edges of the R grid and are applied at each time step in the two regions defined by $R \leq R_-$ and $R \geq R_+$. We chose in this work the third order polynomial form $W_\pm(R) = \xi(R - R_\pm)^3$, proposed by Riss and Meyer,[44] where ξ is a strength parameter. The final analysis is performed by calculating the S-matrix elements $S_{j_2 j_1}(E)$ as:

$$S_{j_2 j_1}(E) = \frac{B_{j_2 j_1}(E)}{a_{j_1}(E)} \sqrt{\frac{k_{j_2}}{\mu}} e^{-ik_{j_2} R_a}, \tag{7}$$

where

$$a_{j_1}(E) = \left(\frac{\mu_R}{k_{j_1}}\right)^{\frac{1}{2}} \int_{-\infty}^{+\infty} G(R)\, e^{-ik_{j_1} R}\, dR \tag{8}$$

is the energy amplitude contained in the initial wave packet for an incoming free wave at energy E,

$$k_{j_i} = \sqrt{2\mu\left(E - \frac{j_i^2}{2I}\right)}, \tag{9}$$

$i = 1, 2$ and

$$B_{j_2 j_1}(E) = \frac{1}{\sqrt{2\pi}} \int_{-\infty}^{+\infty} e^{iEt}\, b_{j_2 j_1}(t)\, \mathrm{d}t. \tag{10}$$

In Eq. (10), the $b_{j_2 j_1}(t) = \langle \varphi_{j_2} | \psi_{j_1}(t) \rangle$ elements are the Fourier transform (time $\leftrightarrow$ energy) of the projection of the TDWP $\psi_{j_1}(R_a, \phi, t)$, taken at the analysis position R_a, on the quantum state $\varphi_{j_2}(\phi)$. The total reaction probability is finally given by

$$P_{j_1}(E) = \sum_{j_2} |S_{j_2 j_1}(E)|^2. \tag{11}$$

Table 1: Parameters in au used in the TDWP calculations to get converged total reaction probabilities over the collision energy range $[0.05 - 0.15]$ eV.

Variable	Value	Description
N_R / N_ϕ	256 / 61	Number of DVR grid points
$R_{\min}$ / $R_{\max}$	-31.56 / 26.15	Minimal and maximal R values
$\phi_{\min}$ / $\phi_{\max}$	$-\pi$ / π	Minimal and maximal ϕ values
σ	1.23	Width of the GWP
E_0	0.011	Mean kinetic energy of the GWP
R_0	-17.36	Center of the GWP
j_1	0	azimuthal quantum number
T	496165	Total propagation time
Δt	3.76	Propagation time step
ξ	0.000005	Strength parameters for the CAP
R_-/ R_+ (au)	-14.42 / 9.25	Location of the CAPs along R
R_d (au)	9.25	Location of the dividing surface

The values of the parameters used in the TDWP calculations are collected in Table 1. The same parameters were used for the two masses. The main issue in TDWP calculations for the low energy domain relates to the ability of the CAP to absorb the wave packet at the edge of the grids, since the associated de Broglie wavelengths are large in this case. Several convergence tests were performed by increasing the length of the absorbing grids and by varying the strength parameter ξ of the CAP. Additional convergence tests were performed for the parameters of the GWP (R_0 and σ) and the location of the analysis line (R_d) to get convergence.

3.1.2 Classical method

10^4 trajectories were run at each energy by numerically solving Hamilton equations[45,46] using the fourth-order Runge-Kutta integrator.[47] Their initial conditions were set at (R_1, ϕ_1, P_1, J_1) with $R_1 = -3$ Å, ϕ_1 randomly selected within the range $[-\pi, \pi]$, $P_1 = k_{j_1}$ [see Eq. (9)] and $J_1 = j_1$. Trajectories were run until R reaches either R_1 (nonreactive paths) or $R_2 = 3$ Å (reactive paths). The values of (ϕ, P, J) at R_2, or back to R_1, are called (ϕ_2, P_2, J_2). We set the time step at 0.1 fs, a standard choice for classical simulations of gas-phase

chemical reactions. The reaction probability was obtained by dividing the number of reactive trajectories by 10^4.

3.1.3 Semiclassical methods: SCIVR and CSMT

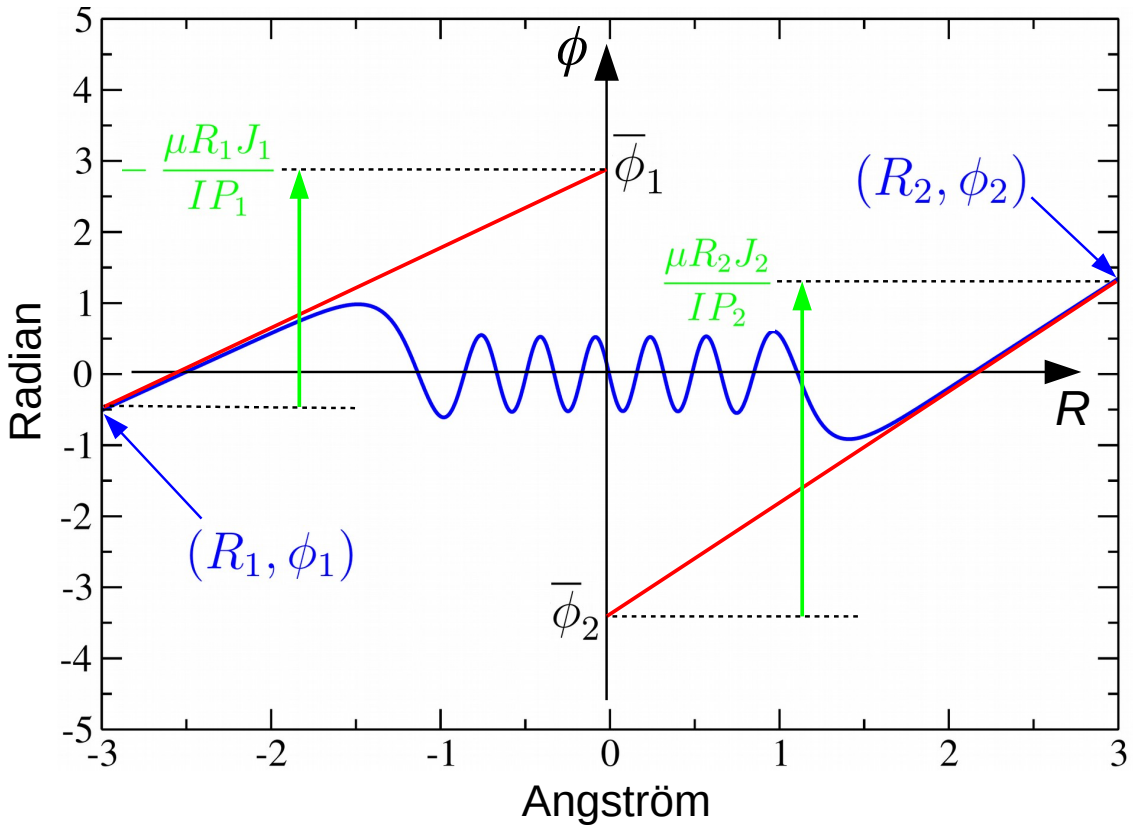

Figure 2: The blue path represents a trajectory going from (R_1, ϕ_1) to (R_2, ϕ_2). The red straight lines on the left and right are tangential to the blue path at (R_1, ϕ_1) and (R_2, ϕ_2), respectively. The green expressions indicate the lengths of the green arrows and, thus, the quantitative link between $(\overline{\phi}_1, \overline{\phi}_2)$ and (ϕ_1, ϕ_2) [see Eqs. (12) and (13)].

Before giving the SCIVR expression of $S_{j_2 j_1}(E)$,[22,27] we need to specify the Miller's shifted angles involved in this expression.[22,48,49] To this aim, we consider in Fig. 2 the blue trajectory run forward in time from (R_1, ϕ_1) to (R_2, ϕ_2) (for the sake of generality, we do not assume that j_1 is 0 in the present part, except at the very end of it). The blue trajectory is such that the four momenta J_1, J_2, P_1 and P_2 are positive; ϕ is indeed increasing at R_1 and R_2, and R

is constantly increasing. The red straight line on the left side is a trajectory run forward in time from (R_1, ϕ_1, P_1, J_1) with $V(R, \phi)$ taken at 0 (we will, however, run it backward in time after defining the shifted angles). The red line is thus tangential to the blue path at (R_1, ϕ_1). This trajectory is stopped at the point of coordinates $(0, \overline{\phi}_1)$ belonging to the ϕ-axis. On the way from $R = R_1$ to $R = 0$, ϕ increases by $[-\frac{\mu R_1 J_1}{I P_1}]$, as indicated in green on the left side of Fig. 2. The mathematical expression of this angular change can be more easily understood if one writes it as the product of $[-\frac{\mu R_1}{P_1}]$, the period of time required to go from $R = R_1$ to $R = 0$, and $\frac{J_1}{I}$, the angular velocity (we recall that $P_1 = \mu \dot{R}_1$ and $J_1 = I\dot{\phi}_1$; note that R_1 is negative while both J_1 and P_1 are positive, so the minus sign in $[-\frac{\mu R_1 J_1}{I P_1}]$ makes positive the variation of ϕ). It is thus clear from Fig. 2 that

$$\overline{\phi}_1 = \phi_1 - \frac{\mu R_1 J_1}{I P_1}. \tag{12}$$

The red line on the right side is a trajectory run backward in time from (R_2, ϕ_2, P_2, J_2) with $V(R, \phi)$ taken at 0. It is thus tangential to the blue path at (R_2, ϕ_2). This trajectory is stopped at the point of coordinates $(0, \overline{\phi}_2)$ belonging to the ϕ-axis. On the way from $R = R_2$ to $R = 0$, ϕ decreases by $[\frac{\mu R_2 J_2}{I P_2}]$, as indicated in green on the right side of Fig. 2 (the mathematical form of this angular change can be justified as previously; since R_2, J_2 and P_2 are all positive, no minus sign is needed in $[\frac{\mu R_2 J_2}{I P_2}]$ to make it positive). From Fig. 2, we clearly have

$$\overline{\phi}_2 = \phi_2 - \frac{\mu R_2 J_2}{I P_2}. \tag{13}$$

$\overline{\phi}_1$ and $\overline{\phi}_2$, also represented for the yellow path in Fig. 1, are Miller's shifted angles.

We are now in a position to specify the type of trajectories involved in the next SCIVR calculations of $S_{j_2 j_1}(E)$. Previously, we introduced the shifted angles by considering that the blue and left red paths in Fig. 2 were run forward in time, while the right red path was run backward in time. For the SCIVR calculations, we will (i) set the values of P_1 and J_1 at k_{j_1} and j_1, respectively, (ii) run the left red path backward in time from $(0, \overline{\phi}_1, k_{j_1}, j_1)$ to

$(R_1, \phi_1, k_{j_1}, j_1)$, (iii) run the blue path forward in time from $(R_1, \phi_1, k_{j_1}, j_1)$ to (R_2, ϕ_2, P_2, J_2), and (iv) run the right red path backward in time from (R_2, ϕ_2, P_2, J_2) to $(0, \overline{\phi}_2, P_2, J_2)$. Time τ will be equal to 0 at $(0, \overline{\phi}_1)$, a given negative value t_1 at (R_1, ϕ_1), a given positive value t_2 at (R_2, ϕ_2), and $[t_2 - \frac{\mu R_2}{P_2}]$ at $(0, \overline{\phi}_2)$.

With this in mind, the SCIVR expression of $S_{j_2 j_1}(E)$ reads[27]

$$S_{j_2 j_1}(E) = \frac{1}{2\pi} \int_{-\pi}^{\pi} d\overline{\phi}_1 \left| \frac{\partial \overline{\phi}_2}{\partial \overline{\phi}_1} \Big|_{j_1} \right|^{1/2} e^{i(\Phi - \pi\bar{\nu}/2)} \rho(\overline{\phi}_1) \tag{14}$$

($\left| \frac{\partial \overline{\phi}_2}{\partial \overline{\phi}_1} \big|_{j_1} \right|$ is the absolute value of $\frac{\partial \overline{\phi}_2}{\partial \overline{\phi}_1} \big|_{j_1}$). $\rho(\overline{\phi}_1)$ is equal to 1 (0) if the blue path is reactive (nonreactive), Φ is given by

$$\Phi = (J_2 - j_2)\, \overline{\phi}_2 + \Omega \tag{15}$$

with

$$\Omega = \Omega_P + \Omega_J, \tag{16}$$

$$\Omega_P = - \int_{t_1}^{t_2} d\tau R \dot{P}, \tag{17}$$

$$\Omega_J = - \int_{t_1}^{t_2} d\tau \phi \dot{J}, \tag{18}$$

and

$$\bar{\nu} = \eta - \chi. \tag{19}$$

Ω is an action integral in the momentum space calculated along the blue path. Ω only depends on the segment of trajectory lying within the interaction region, for outside the latter, P and J are constants of motion. We will call Ω_P and Ω_J the translational and vibrational phases, respectively. η is the Maslov index or number of focal points along the blue path, assuming that the latter is run from $\tau = -\infty$ to $+\infty$, instead of t_1 to t_2. In practice, we analytically extend each blue path from $R = R_1$ to $R = -10^3$ Å and from

$R = R_2$ to $R = 10^3$ Å. Then, we run a second path from the new initial point, with momenta slightly different from k_{j_1} and j_1, up to $R = 10^3$ Å (the momenta are chosen in such a way that both trajectories are at the same energy E). The focal points are the crossing points within (R, ϕ) between the (extended) blue path and the second path, and as mentioned above, η is equal to their number (see Fig. 14 for a pictorial representation of conjugate points). More details on these calculations are given in Sec. III.A.3 of Ref.[28] and in Ref.[27]. χ is 0 (1) if $\frac{\partial \overline{\phi}_2}{\partial \overline{\phi}_1}\Big|_{j_1} \frac{\partial J_2}{\partial \overline{\phi}_1}\Big|_{j_1}$ is positive (negative).[27] The determination of χ requires the calculation of the previous derivatives by running a third trajectory from the same initial conditions as the (non extended) blue path, except that $\overline{\phi}_1$ is increased by a tiny amount (we set it at 10^{-4}). For each values of E, we ran one batch of 10^5 blue paths starting from regularly distributed values of $\overline{\phi}_1$, and two supplementary batches of 10^5 trajectories for the calculation of the pre-exponential factor in Eq. (14) and the indices η, χ and $\bar{\nu}$. Finally, focusing our SCIVR calculations on the case $j_1 = 0$ allowed us to improve their efficiency by exploiting the symmetry of the PES with respect to the R-axis. The details are given in Appendix A.

The CSMT expression of $S_{j_2 j_1}(E)$ is[27,28]

$$S_{j_2 j_1}(E) = \sum_{ReactivePaths} \left[2\pi \left| \frac{\partial J_2}{\partial \overline{\phi}_1}\Big|_{j_1} \right| \right]^{-1/2} e^{i(\Omega - \pi\eta/2 + \pi/4)}. \tag{20}$$

The sum is over the discrete and possibly infinite set of reactive trajectories starting from R_1 with $P_1 = k_{j_1}$ and $J_1 = j_1$, and reaching R_2 with $J_2 = j_2$. The physical meaning of Eq. (20) is as follows. The squared modulus of a given term of the sum is the contribution of the trajectory corresponding to this term to the classical density of probability to go from $J_1 = j_1$ in the reagents to $J_2 = j_2$ in the products.[22,50] In other words, it is the classical statistical weight of the trajectory. In Eq. (20), each trajectory contributing to $S_{j_2 j_1}(E)$ is thus assigned the square root of its statistical weight, as usual in semiclassical mechanics, multiplied by a phase factor accounting for the wave nature of the particles involved in the

collision. The sum in Eq. (20) is the mathematical expression of the superposition principle. CSMT is thus classical mechanics plus the superposition principle. Eq. (20) can be deduced from Eq. (14) by using the stationary phase approximation (SPA).[27,51] Further details on CSMT will be given in Sec. 4.1. We will call $S'_{j_2 j_1}(E)$ the probability amplitude to reform the reagent diatom in the rotational state j_2. The SCIVR and CSMT expressions of $S'_{j_2 j_1}(E)$ are still given by Eqs. (14) and (20), respectively, except that the trajectories taken into account are obviously the nonreactive ones. (Whenever $\frac{\partial J_2}{\partial \overline{\phi}_1}\big|_{j_1}$ is 0 for a given path, the prefactor in Eq. (20) tends to infinity; one may however use SCIVR to calculate the contribution of this path to $S_{j_2 j_1}(E)$, and still use CSMT for the remaining paths).

CSMT was first derived in Refs.[21,24] and soon applied successfully to a collinear inelastic atom-diatom collision in Ref.[22]. SCIVR was originally deduced from CSMT by Fourier transform and application of the stationary phase approximation,[22] but without the phase index $\bar{\nu}$. The latter was introduced in Ref.[27]. Moreover, it has recently been shown that Miller's SCIVR in shifted angles can be obtained from Møller operators and is more efficient than the SCIVR developped within the angles (ϕ_1, ϕ_2).[48,49] This was a bit of a surprise since the angles (ϕ_1, ϕ_2) are those usually used in quantum and classical calculations.

3.2 Results

The $\overline{\phi}_1$ dependence of J_2 is represented in Fig. 3 for $E = 1.2\ E^{\ddagger}_{zpe}$ and $\mu = 19$ amu. We recall that $J_1 = 0$, so the incoming trajectories considered here move parallel to the R-axis in the reagent channel (see the yellow path in Fig. 1). $\overline{\phi}_1$ is thus equal to ϕ_1 [see Eq. (12)]. This will always be so in the following. Owing to the symmetry of the PES with respect to the R-axis (see Fig. 1), J_2 is an odd function of $\phi_1 = \overline{\phi}_1$ (see also Appendix A). J_2 is thus represented in Fig. 3 only within the range $[0, \pi]$. All the trajectories are reactive within the range $[0, \overline{\phi}_{po}[$ and nonreactive within the range $]\overline{\phi}_{po}, \pi]$ (see Fig. 3). The trajectory starting from $\overline{\phi}_{po}$, represented in magenta in Fig. 4, has a special status. It is indeed neither reactive nor nonreactive. Instead, it is trapped by the PO (turquoise segment in Figs. 1 and 4). In

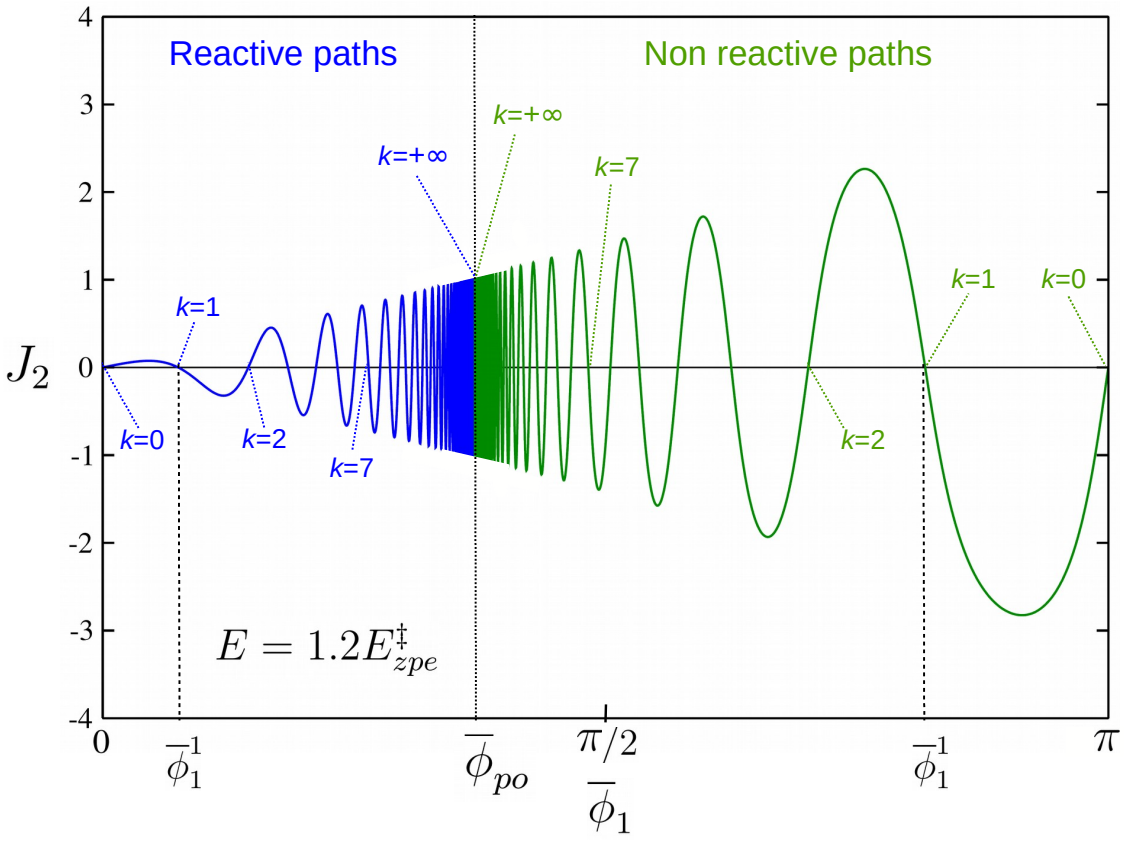

Figure 3: Variation of J_2 in terms of $\overline{\phi}_1$ for the model reaction corresponding to Eqs. (2) and (3), $E = 1.2\ E^{\ddagger}_{zpe}$, and $\mu = 19$ amu. The trajectories leading to $J_2 = 0$ are labeled by the indice k. They start from $(R_1, \overline{\phi}^k_1)$ with $J_1 = 0$ and $P_1 = k_{j_1=0} = \sqrt{2\mu E}$ [see Eq. (9)]. $\overline{\phi}^k_1$ is represented for $k = 1$ on both the reactive and non-reactive sides of $\overline{\phi}_{po}$, the initial angle of the trajectory trapped by the periodic orbit (see Fig. 4). See text for more details.

other words, it approaches the PO indefinitely without ever being able to reach it. This PO is unstable.[33] Consequently, the closer $\overline{\phi}_1$ to $\overline{\phi}_{po}$, the closer the trajectory starting from $\overline{\phi}_1$ passes to the PO, the larger its lifetime in the vicinity of the PO, and the more unstable it is with respect to a tiny variation of its initial conditions. This explains why the local rate of oscillations of J_2 diverges at $\overline{\phi}_{po}$ (see Fig. 3). In the following, we will call *resonant paths* those trajectories trapped in a metastable vibrational motion in the close neighborhood of the PO. The values of $\overline{\phi}_1$ leading to $J_2 = 0$ are denoted $\overline{\phi}^k_1$, where k ranges from 0 to $+\infty$. For example, $\overline{\phi}^1_1$ is represented in Fig. 3 on both the reactive and non-reactive sides of $\overline{\phi}_{po}$

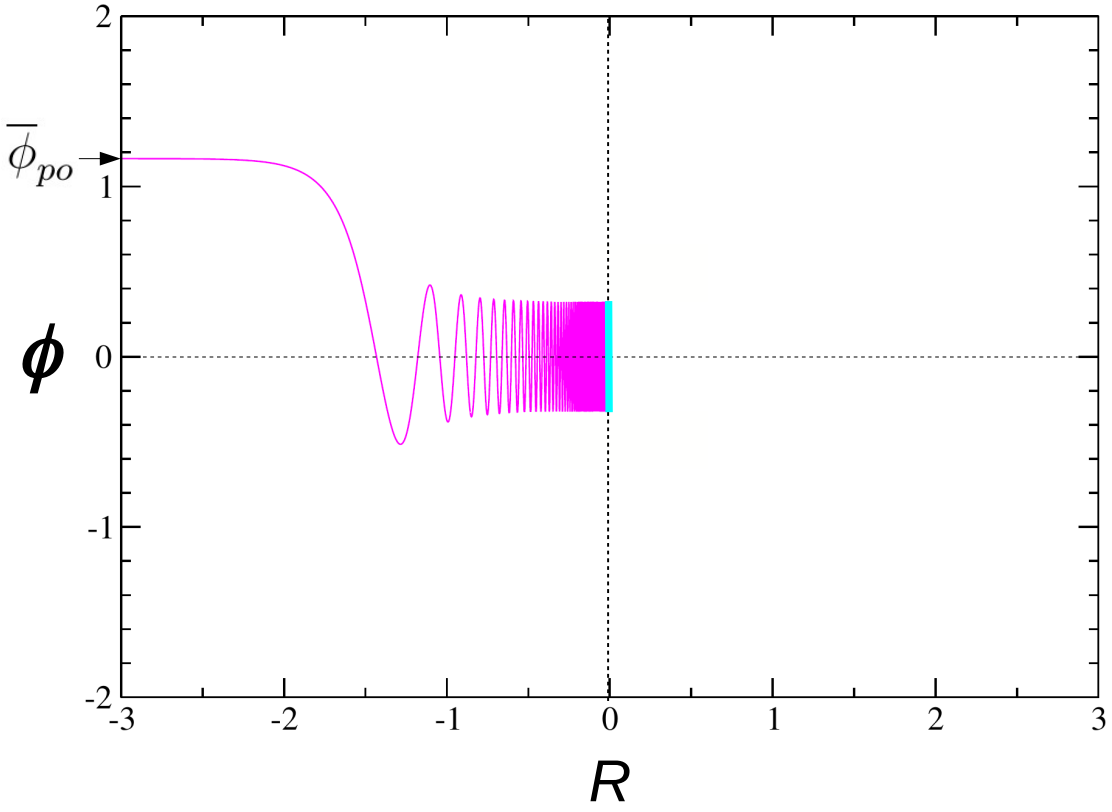

Figure 4: Trajectory starting from $\overline{\phi}_{po}$ (magenta line), trapped by the periodic orbit (turquoise segment), also represented on the PES in Fig. 1. $E = 1.2\ E^{\ddagger}_{zpe}$ and $\mu = 19$ amu.

(the fact that $\overline{\phi}_1^k$ is used for both reactive and nonreactive paths should not be confusing). For reactive paths, $\overline{\phi}_1^0 = 0$ and $\overline{\phi}_1^k$ increases as k increases. For nonreactive paths, $\overline{\phi}_1^0 = \pi$ and $\overline{\phi}_1^k$ decreases as k increases. $\overline{\phi}_1^k$ tends to $\overline{\phi}_{po}$ as k tends to $+\infty$ for both reactive and nonreactive trajectories.

In Fig. 5, the variations with $\overline{\phi}_1$ of the prefactor of the integrand in Eq. (14), and its phase $\Phi - \pi\bar{\nu}/2$, are represented by the orange and green curves, respectively. The two contributions Φ and $-\pi\bar{\nu}/2$ to the phase are also shown (magenta and blue curves, respectively). The calculation of Φ assumes that $j_2 = 0$ [see Eq. (15)]. Careful inspection of the orange, blue and green curves shows that each time the prefactor takes the value 0 (see the downward spikes of the orange curve, one of which is indicated by a small downward arrow), the phase

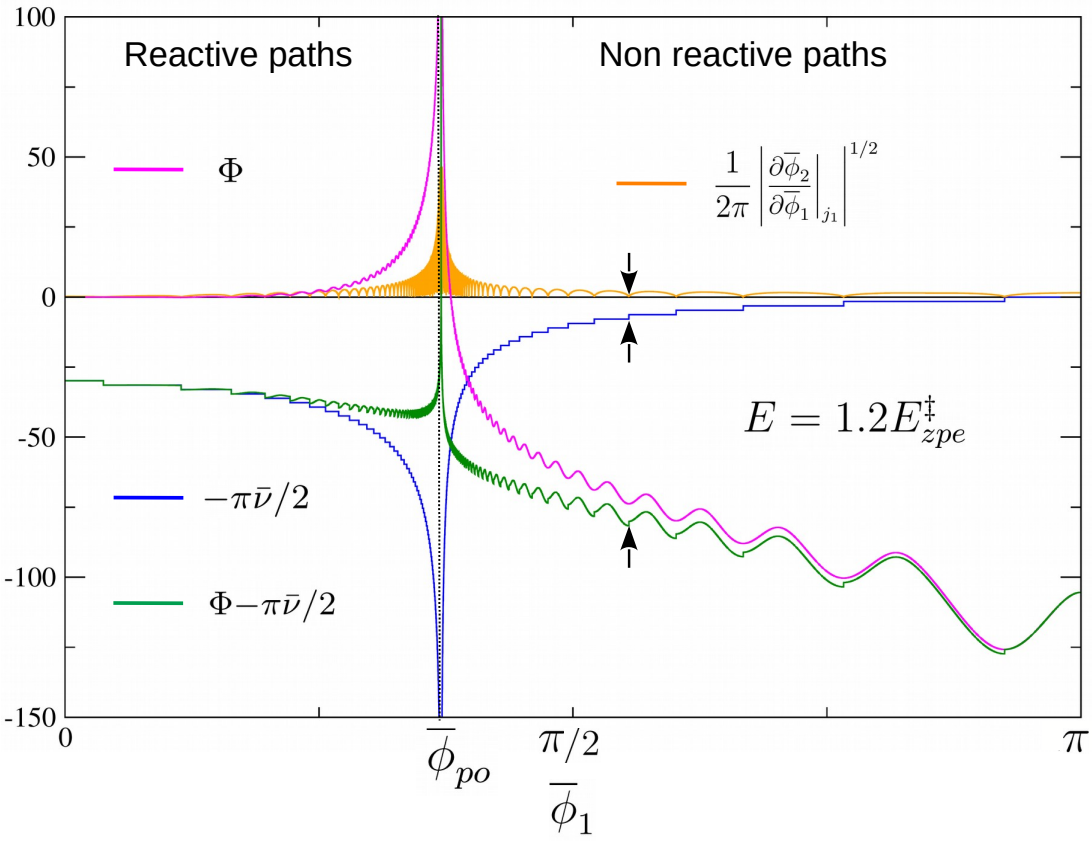

Figure 5: Dependence on $\bar{\phi}_1$ of various terms in the integrand of Eq. (14) for $E = 1.2\ E^{\ddagger}_{zpe}$ and $\mu = 19$ amu: prefactor (orange), Φ (magenta), $-\pi\bar{\nu}/2$ (blue) and the overall phase $\Phi - \pi\bar{\nu}/2$ (green = magenta+blue). Φ is calculated for $j_2 = 0$ [see Eq. (15)].

jumps by $\pi/2$ (see the two small upward arrows below the downward arrow). The sign of the jump as $\bar{\phi}_1$ increases is negative (positive) for the reactive (nonreactive) paths. These jumps are necessary to make the integrand in Eq. (14) continuous. All the curves diverge at $\bar{\phi}_{po}$, due to the resonant paths (we will come back to this point in Sec. 4). The values of $\bar{\phi}_1$ very close to $\bar{\phi}_{po}$ cause the integrand of Eq. (14) to oscillate very strongly, and with a very large amplitude. Thus, the contribution of these values to the integral of Eq. (14) is difficult to numerically estimate. We thus ignored those trajectories for which $\pi\bar{\nu}/2$ is larger than 150. It is clear from Fig. 5 that these paths represent a very small part of the whole set of trajectories run, so the contribution of the former to $S_{j_2 j_1}(E)$ is expected to be negligible.

In principle, S-matrix elements should be normalized to unity, i.e., $N_{j_1} = \Sigma_{j_2}|S_{j_2 j_1}(E)|^2 +$

$|S'_{j_2 j_1}(E)|^2 = 1$. This is indeed what we previously found for an inelastic collision with no trapped PO (N_{j_1}, then, reduces to $\Sigma_{j_2}|S_{j_2 j_1}(E)|^2$).[27] For the present model reaction, however, Eq. (14) leads to values of N_{j_1} scattered within the range $[0.8, 2]$, depending on E (note that the code used for the present study is the one used to obtain the results of Ref.[27]). We attribute this lack of normalization to the presence of the PO, as such orbits are well known to strongly affect the accuracy of semiclassical calculations.[29] In order to improve the consistency of our predictions, we thus divided S-matrix elements by $N_{j_1}^{1/2}$. This pragmatic procedure does not work miracles, but it necessarily ensures normalization to unity.

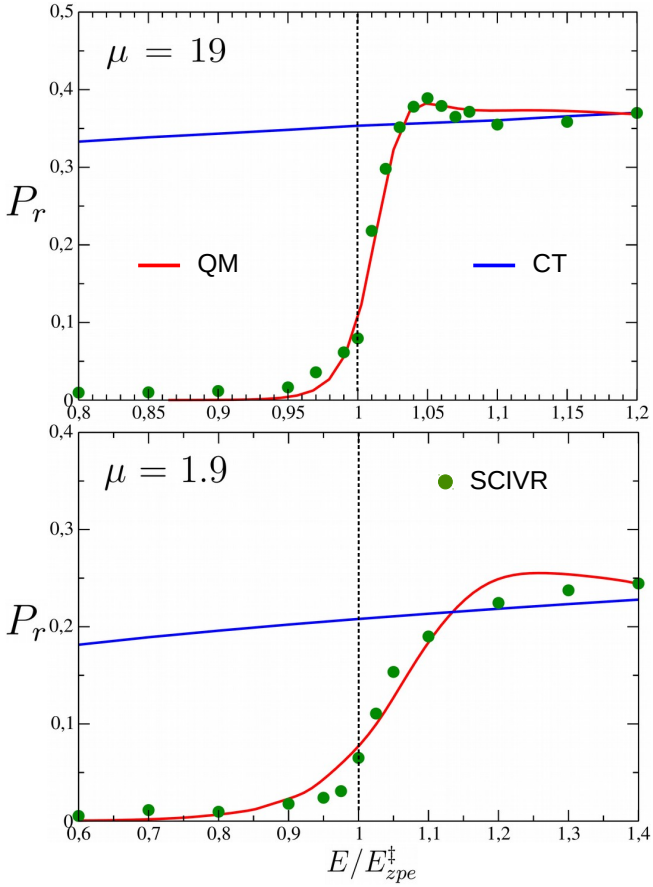

Figure 6: Energy dependence of the reaction probability around the threshold, in unit of $E^{\ddagger}_{zpe}$. The upper (lower) panel corresponds to the heavy (light) mass. The red and blue curves are obtained from quantum mechanical (QM) and classical trajectory (CT) calculations, respectively, while the green circles are obtained by rescaling SCIVR results by a factor of one half. See text for more details.

The energy dependence of the reaction probability P_r around the threshold is represented

in Fig. 6 for both the heavy mass (upper panel) and the light mass (lower panel). The red and blue curves were obtained from quantum mechanical (QM) and classical trajectory (CT) calculations, respectively (in general, the acronym QCT (Q referring to quasi) means that the reagents are prepared with a given quantized vibrational energy, usually the ZPE, which is not the case here since we are dealing with a rigid rotor). The classical energy threshold (not visible in Fig. 6) is equal to 0. The quantum energy threshold appears to be well defined by Eq. (1) since the reactivity starts to be significant at $E = E^{\ddagger}_{zpe}$. The green circles were deduced from SCIVR calculations in the following way: the true SCIVR probabilities, not represented in Fig. 6, were found equal to about twice the quantum probabilities for both masses (we carefully checked than no factor 2, artificially doubling the reaction probability, was introduced by mistake in our code). For clarity's sake, the probabilities corresponding to the green circles in Fig. 6 were therefore set to half of their actual values. This rescaling shows unambiguously that, even if SCIVR overestimates the reactivity, it nevertheless reproduces very well the (nearly) sigmoidal shape of the quantum probability around the threshold for each of the two masses. The goal of the next section is to explain the origin of the threshold, its value around $E^{\ddagger}_{zpe}$, and its shape.

4 Analysis of the results

In the present part, we focus on the S-matrix elements $S_{00}(E)$ and $S'_{00}(E)$ for two reasons. The first one is that in the vicinity of the threshold, the evolutions with E of $|S_{j_20}(E)|^2$ and $|S'_{j_20}(E)|^2$ for $j_2 \neq 0$ are found from quantum calculations to be similar to those of $|S_{00}(E)|^2$ and $|S'_{00}(E)|^2$ (not shown). The second reason is that the analytical formulation presented later on requires that j_2 be 0. In addition to the energy $E = 1.2E^{\ddagger}_{zpe}$, we consider hereafter the threshold energy $E = E^{\ddagger}_{zpe}$ and the energy $E = 0.8E^{\ddagger}_{zpe}$, symmetrical of the first one with respect to the threshold.

4.1 Qualitative analysis

The semiclassical method best suited to the analysis of the threshold is CSMT. Within this approach, $S_{j_2 j_1}(E)$ is given by Eq. (20). However, in the particular case that interests us, i.e., $j_2 = j_1 = 0$, Eq. (20) can be rewritten as

$$S_{00}(E) = \sum_{k=0}^{+\infty} \gamma_k \left[2\pi \left| \frac{\partial J_2}{\partial \overline{\phi}_1} \Big|_k \right| \right]^{-1/2} e^{i\Psi_k}. \tag{21}$$

with

$$\Psi_k = \Omega_k - \pi\eta_k/2 + \pi/4. \tag{22}$$

The k^{th} term of the sum is calculated for $\overline{\phi}_1^k$ lower than $\overline{\phi}_{po}$ (see Fig. 3 and the related discussion; we recall that the $\overline{\phi}_1^k$'s are those values of $\overline{\phi}_1$ leading to $J_2 = 0$). $S'_{00}(E)$ is determined in the same way, but from the $\overline{\phi}_1^k$'s larger than $\overline{\phi}_{po}$. γ_k is equal to 1 for $k = 0$, and 2 for $k > 0$. $\frac{\partial J_2}{\partial \overline{\phi}_1}\big|_k$ means value of $\frac{\partial J_2}{\partial \overline{\phi}_1}\big|_{j_1=0}$ at $\overline{\phi}_1^k$. Eq. (21) is straightforwardly deduced from Eq. (20) by taking into account the symmetry properties discussed in Appendix A.

In Fig. 7, the values Ω_{Pk} of the translational phase, and Ω_{Jk} of the vibrational phase, are represented in terms of $\overline{\phi}_1^k$ for $E = 0.8E^{\ddagger}_{zpe}$ and $\mu = 19$. Ω_{Pk} and Ω_{Jk} correspond to the blue circles and blue squares, respectively. We recall that Ω_P and Ω_J are given by Eqs. (17) and (18), and $\Omega_{Pk} + \Omega_{Jk} = \Omega_k$. In addition, the Maslov index η_k, multiplied by $-\pi/2$, is also represented in Fig. 7 by the upward green triangles. Note that the closer the filled symbols to the vertical dashed line, the more they overlap. It is indeed clear from Fig. 3 that the larger k, the lower the difference $(\overline{\phi}_1^{k+1} - \overline{\phi}_1^k)$. We will now analyse the variations of Ω_{Pk}, Ω_{Jk} and η_k in terms of $\overline{\phi}_1^k$, from which we will deduce that of the overall phase Ψ_k. We start with Ω_{Jk}, because its study is a little simpler than that of Ω_{Pk}, we continue with η_k, then with Ω_{Pk}, and we end with Ψ_k.

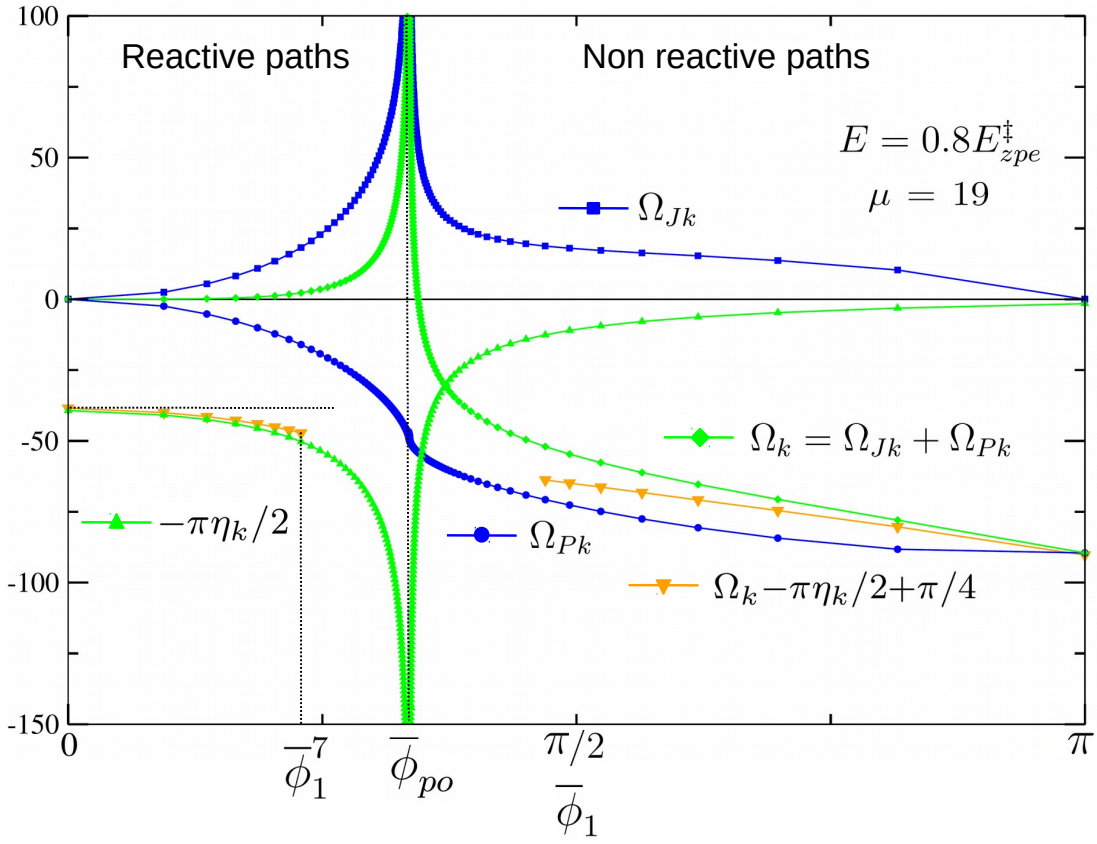

Figure 7: Representation of Ω_{Pk} (blue circles), Ω_{Jk} (blue squares), Ω_k (green diamond), $-\pi\eta_k/2$ (upward green triangles), and the overall phase $\Psi_k = \Omega_k - \pi\eta_k/2 + \pi/4$ in Eq. (21) (downward orange triangles). The segments joining the symbols are guides for the eyes, and this will be so further below for all the figures based on CSMT calculations. The sum of the blue symbols gives the green diamonds, while the sum of the green symbols gives the downward orange triangles. The overall phase is only represented for $k \leq 7$ in order to emphasize that far enough from the trapping angle $\overline{\phi}_{po}$, the slope of the overall phase is negative from left to right.

4.1.1 Vibrational phase Ω_{Jk}

The reactive path starting from $\overline{\phi}_1^7 = 0.7196$ (see Fig. 7) is represented in Fig. 8 in the (ϕ, J) plane. The blue dot corresponds to the starting point (at $R = R_1 = -3$ Å) while the red dot corresponds to the end point (at $R = R_2 = 3$ Å). Note that both J_1 and J_2 are zero, as is the case for all the trajectories contributing to Eq. (21). Since for positive (negative) values of J, ϕ increases (decreases), the path is run clockwize. Therefore, when ϕ is negative

(positive), J is increasing (decreasing), in such a way that $-\phi\dot{J}$ is always positive or zero. Consequently, Ω_{Jk} is necessarily positive (see Fig. 7). We can see this even more directly if, using the integration-by-part formula, one expresses Ω_J [see Eq. (18)] as

$$\Omega_J = \int_{t_1}^{t_2} d\tau J\dot{\phi} - (J_2\phi_2 - J_1\phi_1) = \int_{t_1}^{t_2} d\tau \frac{J^2}{I} = \int_{\phi_1}^{\phi_2} J d\phi. \tag{23}$$

The second equality, which comes from the fact that $J = I\dot{\phi}$ and $J_1 = J_2 = 0$, confirms our previous statement. Moreover, the third equality shows that Ω_J is the cumulative area within the (ϕ, J) plane of all the loops performed between the blue and red dots (see Fig. 8; the loops are elliptic within the channel). It is clear that the closer $\overline{\phi}_1^k$ to $\overline{\phi}_{po}$, the longer the time spent by the system within the channel, the larger the number of loops, and the larger Ω_{Jk}. This explains why the Ω_{Jk}'s involve an upward peak centered at $\overline{\phi}_{po}$ (see Fig. 7). Finally, $\dot{J}$ is 0 all along the trajectories starting from 0 and π (see Fig. 1). For these two angles, $\Omega_J = \Omega_{J0}$ is thus zero (see Fig. 7). In conclusion, Ω_{Jk} increases monotonically from 0 at $\overline{\phi}_1^0 = 0$ to $+\infty$ at $\overline{\phi}_{po}$, and decreases monotonically from $+\infty$ at $\overline{\phi}_{po}$ to 0 at $\overline{\phi}_1^0 = \pi$. Therefore, the Ω_{Jk}'s involve an upward peak centered at $\overline{\phi}_{po}$, the tip of which is due to resonant paths.

4.1.2 Maslov index η_k

As will be shown in Sec. 4.2.1, η_k is roughly equal to twice the number of vibrational periods spent by the k^{th} trajectory within the channel, i.e., twice the number of loops shown in Fig. 8. Since the number of loops, and thus η_k, tends to $+\infty$ as $\overline{\phi}_1^k$ tends to $\overline{\phi}_{po}$, the values of $-\pi\eta_k/2$ involve a downward peak (see the upper green triangles in Fig. 7).

4.1.3 Translational phase Ω_{Pk}

The three reactive trajectories starting from $\overline{\phi}_1^0 = 0$, $\overline{\phi}_1^7 = 0.7196$, and $\overline{\phi}_1^\infty = \overline{\phi}_{po} - \epsilon$ (ϵ being positive and infinitesimal) are represented in the (R, P) plane by the blue curves in Fig. 9.

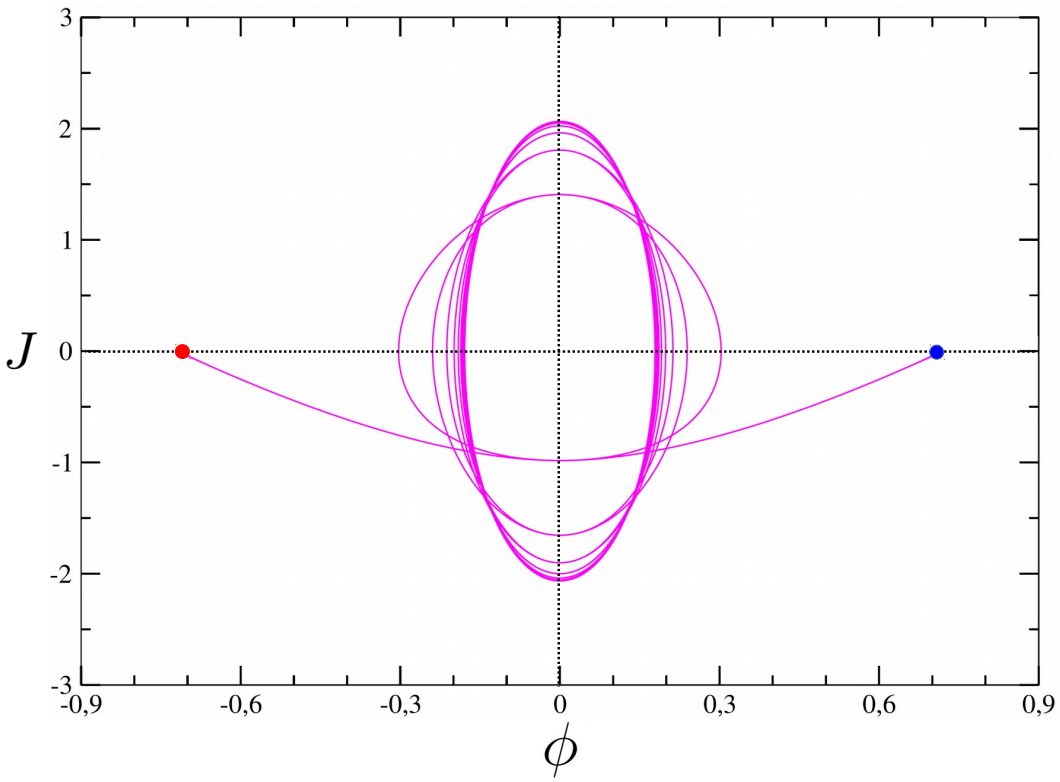

Figure 8: Projection on the (ϕ, J) plane of the reactive path starting from $\overline{\phi}_1^7$ (see Fig. 7). $E = 0.8E_{zpe}^{\ddagger}$ and $\mu = 19$. Blue dot: starting point, at $R = R_1 = -3$; red dot: end point, at $R = R_2 = 3$ Å.

The first one, labeled $k = 0$, follows the R-axis (see Fig. 3) with a constant momentum $P = P_1 = P_2 = (2\mu E)^{1/2}$ [see Eq. (3)]. Equation (17) shows that Ω_{P0} is thus zero (see Fig. 7). Along the second trajectory, labeled $k = 7$, P decreases by about a quarter before returning to its starting value. Using again the integration-by-part formula, Ω_P [see Eq. (18)] can be written as

$$\Omega_P = \int_{R_1}^{R_2} P dR - (P_2 R_2 - P_1 R_1). \tag{24}$$

$\int_{R_1}^{R_2} P dR$ is the area between the blue curve labeled $k = 7$, the magenta axis, and the vertical edges of the frame. $(P_2 R_2 - P_1 R_1)$ is the rectangular area defined by the upper blue line, the magenta axis, and the vertical edges of the frame. Ω_{P7} is thus given by minus the area

between the two upper blue lines, found equal to -16 (see the eight blue circle from the left in Fig. 7). The third blue path, labeled $k = +\infty$, starts from $\overline{\phi}_1^{\infty} = \overline{\phi}_{po} - \epsilon$ and follows the trapped trajectory for an infinite time before crossing the TS, then takes the same time to move away from the TS and reach the products. One notes the symmetry of the projection of this path with respect to the P-axis (vertical green axis; see Fig. 9), and the fact that P tends to 0 at the TS. $\Omega_{P\infty}$ is equal to minus the area between the upper and lower blue lines, found roughly equal to -50 (see Fig. 7). The projections in the (R, P) plane of two nonreactive paths are also displayed in Fig. 9 (orange curves). The path labeled $k = +\infty$ starts from $\overline{\phi}_1^{\infty} = \overline{\phi}_{po} + \epsilon$ and follows the trapped trajectory for an infinite time until "touching" the TS without being able to cross it. The trajectory then needs the same time to move away from the TS and turn back to the reagents. Thus, this path overlaps the blue path labeled $k = +\infty$ from the reagents onto the TS (we had to slightly shift the orange and blue paths relative to each other to distinguish them). Then, the two paths separate symmetrically with respect to the origin of the (R, P) plane. Eq. (24) (reformulated for the present path) shows that $\Omega_{P\infty}$ is equal to the area encompassed by the orange path labeled $k = +\infty$ and the left vertical edge of the frame, minus the area of the square defined by the green lines, the upper blue line, and the left vertical edge of the frame. $\Omega_{P\infty}$ is thus equal to -50, just as for the blue trajectory labeled $k = +\infty$. The second nonreactive path labeled $k = 0$ starts from $\overline{\phi}_1^0 = \pi$. The value of R at the turning point is much lower than for the previous orange path (see Fig. 9), thus implying a significantly lower value of Ω_{P0} (-89.5). In conclusion, the fact that for reactive paths, the value of P at the TS decreases when $\overline{\phi}_1^k$ increases, and for nonreactive paths, the value of R at the turning point decreases when $\overline{\phi}_1^k$ increases, makes Ω_{Pk} a monotonously decreasing function from 0 to π (see Fig. 7).

4.1.4 Overall phase Ψ_k

Let us concentrate on $\Omega_k = \Omega_{Jk} + \Omega_{Pk}$ for the height reactive trajectories starting from $\overline{\phi}_1^k$, $k = 0, ..., 7$ (see the left side of Fig. 7). Since Ω_{Jk} and Ω_{Pk} have nearly the same absolute

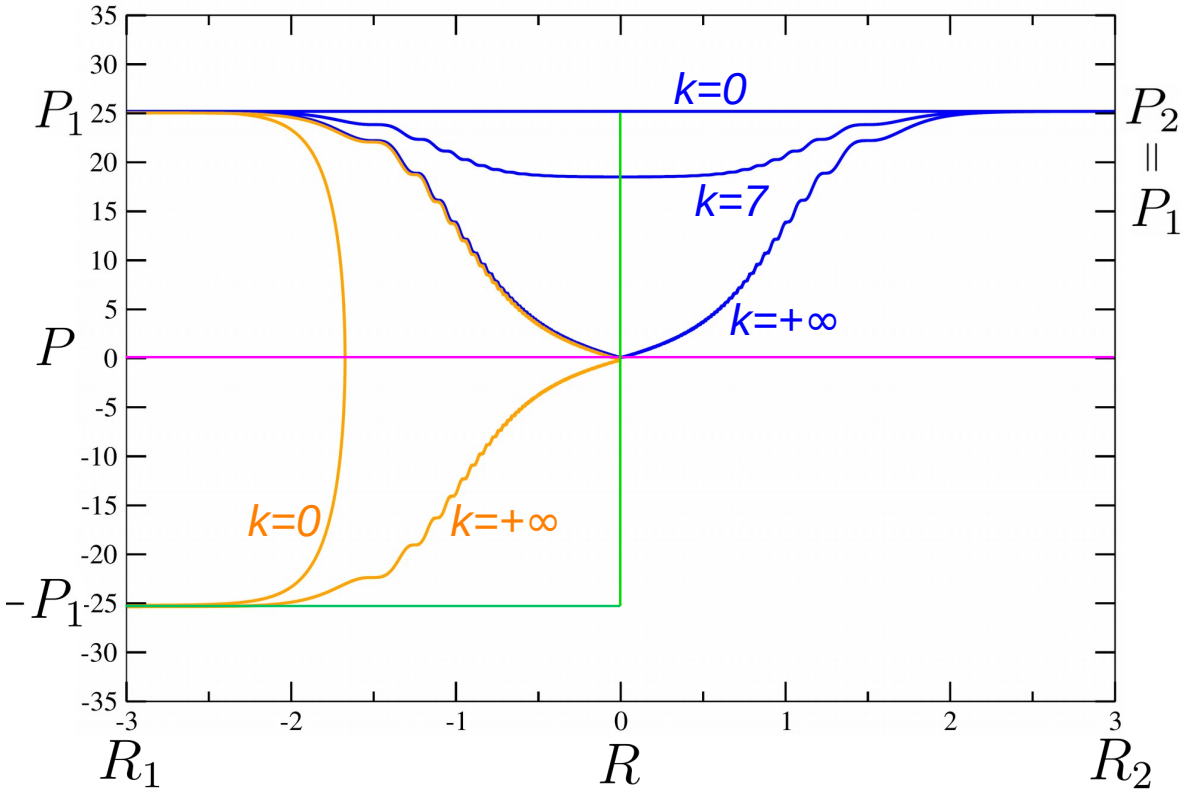

Figure 9: Projection on the (R, P) plane of the reactive paths starting from $\overline{\phi}_1^0 = 0$, $\overline{\phi}_1^7 = 0.7196$ and $\overline{\phi}_1^\infty = \overline{\phi}_{po} - \epsilon$ (blue lines) and the nonreactive paths starting from $\overline{\phi}_1^\infty = \overline{\phi}_{po} + \epsilon$ and $\overline{\phi}_1^0 = \pi$ (orange lines). $E = 0.8E_{zpe}^{\ddagger}$ and $\mu = 19$. Since $\overline{\phi}_1^\infty$ "touches" $\overline{\phi}_{po}$ for both the blue and the orange lines labeled $k = +\infty$, they virtually overlap from (R_1, P_1) to (0,0), while their second halves are symmetric with respect to (0,0). For the reactive paths, the quantity $P_2R_2 - P_1R_1$ is the area of the rectangle defined by the magenta line, the blue line labeled $k = 0$, and the vertical edges of the frame. For the nonreactive paths, $P_2R_2 - P_1R_1$ is the area of the square defined by the green lines, the blue line labeled $k = 0$, and the left vertical edge of the frame. The two areas are identical. This drawing is used in the text to explain why in Fig. 7, the Ω_{Pk}'s continuously decrease from left to right.

values, but opposite signs, Ω_k is close to 0. The overall phase $\Psi_k = \Omega_k - \pi\eta_k/2 + \pi/4$ of Eq. (21) (downward orange triangles), equal to the sum of the two green curves in Fig. 7 plus $\pi/4$, is thus close to $-\pi\eta_k/2$ (upward green triangles) and the orange curve that fits them decreases. As for the height nonreactive trajectories starting from $\overline{\phi}_1^k$, $k = 0, ..., 7$ (see the right side of Fig. 7), both Ω_{Jk} and Ω_{Pk} decrease as $\overline{\phi}_1^k$ increases while $-\pi\eta_k/2$ is almost flat in

comparison. Therefore, Ψ_k decreases. To sum up, the phase Ψ_k of Eq. (21) decreases within the ranges $\sim [0, \pi/5]$ and $\sim [\pi/2, \pi]$, i.e., for the nonresonant trajectories, and we have found that this behaviour is independent on the value of E within the range $[0.8E^{\ddagger}_{zpe}, 1.2E^{\ddagger}_{zpe}]$.

In contrast, we now show that the behaviour of Ψ_k changes with E for the resonant paths, i.e., for the values of $\overline{\phi}_1^k$ close to $\overline{\phi}_{po}$. The reason is as follows. First, Ω_{Jk} tends to $+\infty$ as $\overline{\phi}_1^k$ tends to $\overline{\phi}_{po}$ while Ω_{Pk} retains a finite value that can be considered constant as compared to Ω_{Jk} (compare the two blue curves in Fig. 7 around $\overline{\phi}_{po}$). Second, for the resonant paths, nearly all the energy E is in the vibrational motion within the channel, and the average area of a single loop, call it $A(E)$, increases with E (in Sec. 4.2, we will derive the analytical expression of $A(E)$ for a channel of harmonic section). Third, we know that Ω_{Jk} is equal to the sum of $A(E)$ over the loops; but we have seen previously that the number of loops is roughly equal to half the Maslov index η_k (see Sec. 4.1.2), so Ω_{Jk} can be approximated by $A(E)\eta_k/2$. Therefore, the k-dependent part $[\Omega_{Jk} - \pi\eta_k/2]$ of Ψ_k is equal to $\sim [A(E) - \pi]\eta_k/2$. When E tends to 0, the area of the loops are negligible and so is $A(E)$. Consequently, the previous phase reduces to $-\pi\eta_k/2$ which tends to $-\infty$ as $\overline{\phi}_1^k$ tends to $\overline{\phi}_{po}$ (see the upward green triangles in Fig. 7). Thus, the overall phase Ψ_k is expected to involve a downward peak centered at $\overline{\phi}_{po}$. When E increases and takes the value satisfying the constraint $A(E) = \pi$, the k-dependent part of Ψ_k is 0 and no peak is expected. When E continues to increase, $A(E)$ gets larger than π, and $[A(E) - \pi]\eta_k/2$ tends to $+\infty$ as $\overline{\phi}_1^k$ tends to $\overline{\phi}_{po}$. An upward peak is then expected.

Now, what can we say about the solution of the equation $A(E) = \pi$? Since resonant trajectories spend most of their long stay in the interaction region vibrating like the PO, the average area $A(E)$ of a single loop is very close to $A^{\ddagger}(E)$, the area $\oint J d\phi$ inside the PO. Moreover, it is well known that the vibrational action $n^{\ddagger}(E)$ along the PO, plus $\frac{1}{2}$, is equal to $A^{\ddagger}(E)$ divided by Planck constant h (see Chapter 7.1.1 in Ref.[52]). Since we are working

in $\hbar$ unit, $h = 2\pi$, and the previous statement becomes

$$n^{\ddagger}(E) + \frac{1}{2} = \frac{A^{\ddagger}(E)}{2\pi}. \tag{25}$$

Now, if $A^{\ddagger}(E) = A(E) = \pi$, Eq. (25) implies

$$n^{\ddagger}(E) = 0. \tag{26}$$

However, the vibrational action is the classical analog of the vibrational quantum number,[51,52] so the solution of Eq. (26) is necessarily

$$E = E^{\ddagger}_{zpe}. \tag{27}$$

Eq. (25), together with the constraint that $n^{\ddagger}(E)$ be an integer, is nothing but the *Bohr-Sommerfeld quantization rule*[51,52] applied to the activated complex (or the TS). To recap, the Ψ_k's are expected to involve a downward peak below $E^{\ddagger}_{zpe}$, no peak at $E^{\ddagger}_{zpe}$, and an upward peak above $E^{\ddagger}_{zpe}$.

These predictions are indeed confirmed by Figs. 10 to 12 which display the Ψ_k's (orange circles) for the three energies $0.8E^{\ddagger}_{zpe}$, $E^{\ddagger}_{zpe}$ and $1.2E^{\ddagger}_{zpe}$ and $\mu = 19$ (contrary to Fig. 7, the present figures show the phase for all the values of $\overline{\phi}^k_1$ going from 0 to π). As expected, the phases form a sharp peak directed downward below $E^{\ddagger}_{zpe}$ (Fig. 10), upward above $E^{\ddagger}_{zpe}$ (Fig. 12) and there is no peak at $E^{\ddagger}_{zpe}$ (Fig. 11). Note that in Fig. 11, the orange circles scattered over a dozen units along the dotted line correspond to very unstable trajectories. Consequently, their positions are quite inaccurate. Owing to the smooth alignment of the circles located close to the dotted line without overlapping it (these dots correspond to more stable trajectories), we will assume that more exact calculations, beyond reach with current computers, would smooth the alignment of the circles up to $\overline{\phi}_{po}$ (we will analytically validate this assumption in Sec. 4.2 for reactive paths). Anyway, the important observation here is

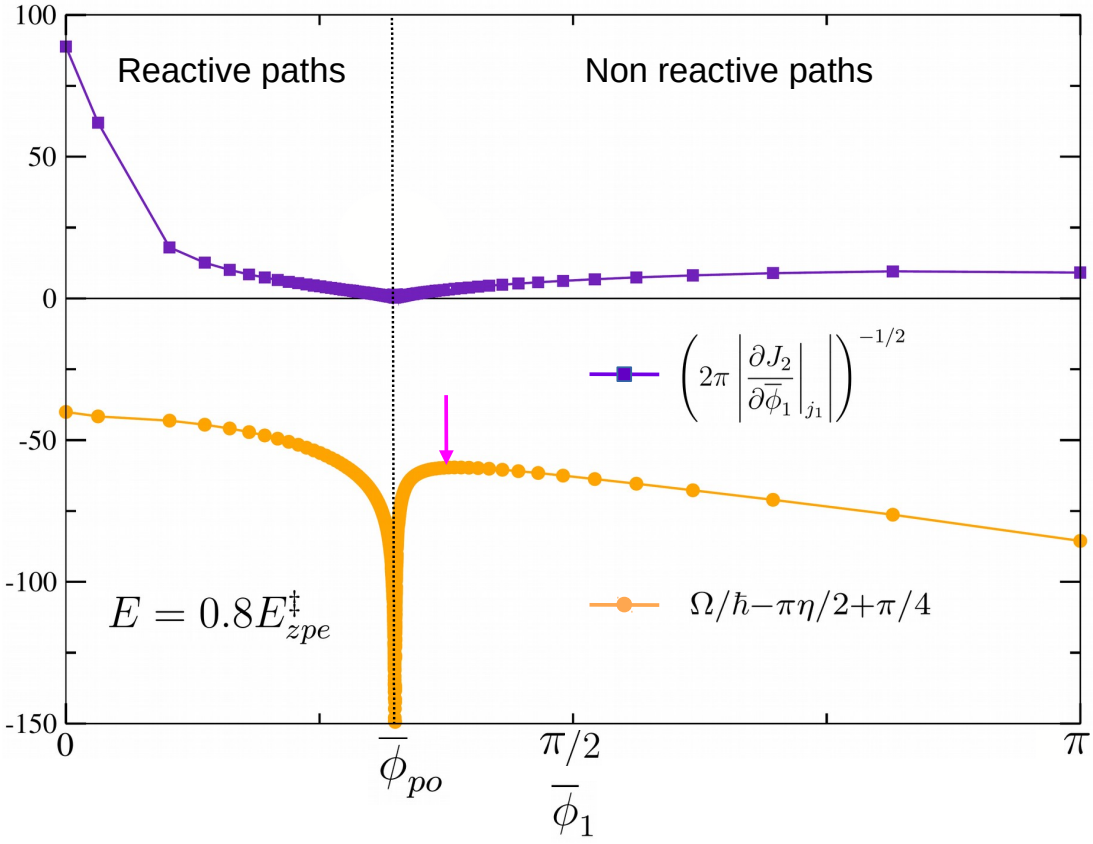

Figure 10: Prefactor (indigo squares) and phase (orange circles) for each term of the CSMT expression of $S_{00}(E)$ and $S'_{00}(E)$ [see Eq. (21)]. $\mu = 19$. The magenta arrow indicates the stationary phase on the nonreactive side.

that the orientation of the phase peak switches at $E^{\ddagger}_{zpe}$ from down to up. In addition, we have seen previously that the phase monotonically decreases within the ranges [0, $\sim \pi/5$] and [$\sim \pi/2$, π] (see the downward orange triangles in Fig. 7 as well as the orange circles in Figs. 10 to 12).

Combined, these two properties have a major effect on the reaction probability for the following reason: below $E^{\ddagger}_{zpe}$, the phase involves a stationary point on the nonreactive side of $\overline{\phi}_{po}$, as indicated by the magenta arrow in Fig. 10, while the phase decreases monotonously on the reactive side of $\overline{\phi}_{po}$. On the other hand, the opposite is observed above $E^{\ddagger}_{zpe}$: the stationary phase is indeed on the reactive side of $\overline{\phi}_{po}$, as indicated by the magenta arrow in Fig. 12, while the phase decreases monotonously on the nonreactive side of $\overline{\phi}_{po}$.[53] However,

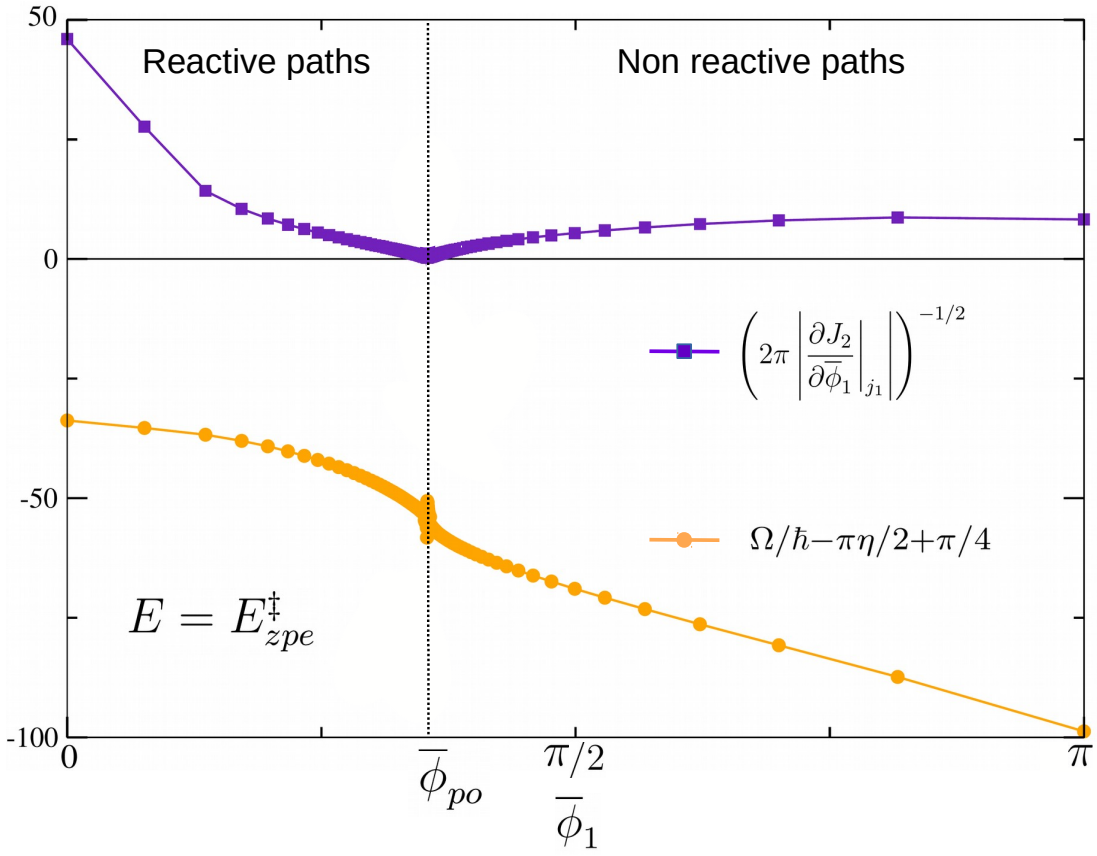

Figure 11: Same as Fig. 10, with the difference that the stationary phase is at $\overline{\phi}_{po}$ for both reactive and nonreactive paths.

the squared modulus of a sum of complex numbers is the greater the closer their phases are to each other, because when this is the case, the complex numbers interfere in a constructive way. Therefore, if the Ψ_k's involve a stationary point, the phases around the stationary point lead to constructive interferences, while if the Ψ_k's are monotonously decreasing, the interferences are generally destructive (see further on the discussions around Figs. 13 and 21). Consequently, at 0.8 $E^{\ddagger}_{zpe}$, where the phases decrease monotonously for the reactive paths while there is a stationary phase for the nonreactive paths (see Fig. 10), $|S_{00}(E)|^2$ and $|S'_{00}(E)|^2$ are expected to be small and large, respectively. Conversely, at $1.2E^{\ddagger}_{zpe}$, where there is a stationary phase for the reactive paths while the phases decrease monotonously for the nonreactive paths (see Fig. 12), the reverse is expected, i.e., $|S_{00}(E)|^2$ and $|S'_{00}(E)|^2$

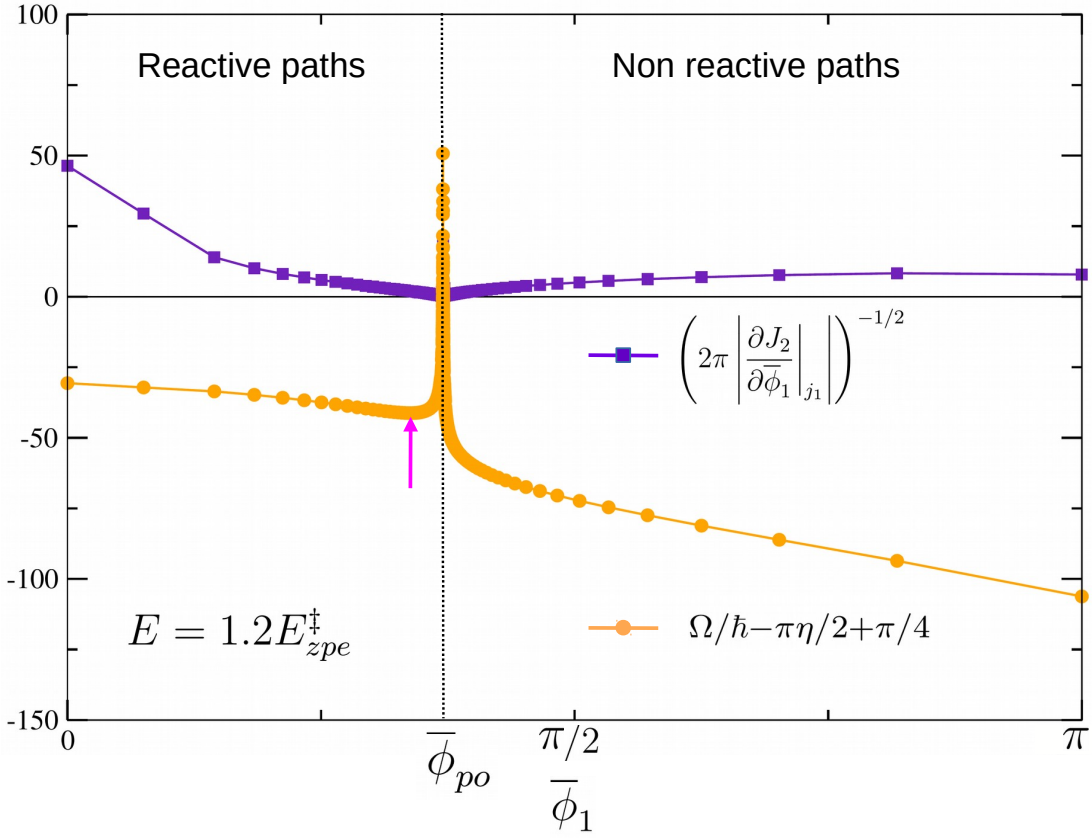

Figure 12: Same as Fig. 10, with the difference that the magenta arrow indicates the stationary phase on the reactive side.

are expected to be large and small, respectively. Since the same trends are also expected for the remaining state-to-state populations (see the first paragraph of the present section), the probability of reaction necessarily has a threshold at $\sim E^{\ddagger}_{zpe}$. This achieves the justification of a chemical reaction threshold in terms of interferences between probability amplitudes carried by classical paths. The threshold constraint on bending across the interaction region is thus properly built into semiclassical mechanics.

Last but not least, at $E^{\ddagger}_{zpe}$ (see Fig. 11), the phases are identical for the infinite number of dots that overlap at $\overline{\phi}_{po}$ (assuming, as previously stated, that they form a smooth line around $\overline{\phi}_{po}$). $S_{00}(E)$ and $S'_{00}(E)$ are thus given by a sum of complex amplitudes [see Eq. (21)] among which an infinite number, corresponding to the large k's (resonant paths), have the

same phase. In other words, right at $E_{zpe}^{\ddagger}$, we have a resonant phase-matching, or resonance. This finding, which we have seen is intimately related to Eq. 25, bears similarities with previous findings by Pollak and Child[33,54] on quantal resonances above threshold.[55] Note that the prefactor, represented in Figs. 10 to 12 by the indigo squares, tends to 0 at $\overline{\phi}_{po}$ whatever the energy. Therefore, at $E_{zpe}^{\ddagger}$, both $S_{00}(E)$ and $S'_{00}(E)$ are given by a finite sum of complex numbers with varying phases, corresponding to k lower than a few tens, plus an infinite sum of complex numbers with nearly equal phases and a modulus vanishing for huge k's. It is shown in Appendix B that this modulus is approximately proportional to $1/k^{3/2}$, the sum of which (from $k > 0$) is convergent (the developments of Appendix B rely on those of Sec. 4.2.1). This explains why $|S_{00}(E)|^2$ and $|S'_{00}(E)|^2$ do not diverge at the threshold.

On the other hand, the notion of resonance is not relevant apart from the threshold energy. As shown further below, only a few tens of trajectories with phases distributed around the stationary phase contribute to the reactivity, against an infinite number at $E_{zpe}^{\ddagger}$ as we have just seen.

4.1.5 Folding functions

It is both instructive with respect to what as already been said, and aesthetically pleasing, to visualize the effect of the peak reorientation on $S_{00}(E)$ and $S'_{00}(E)$. To this aim, we define the *folding function* $F(N)$ as the right-hand-side of Eq. (21), build from reactive paths, limited to the $N + 1$ first values of k. Then, we consider the path followed by $F(N)$ in the complex plane when N is increased from 0 to $+\infty$, where $F(N)$ tends to $S_{00}(E)$ (in all rigor, $F(N)$ is a sum; the word "function" is best suited to the SCIVR analog of $F(N)$ discussed in Appendix C). This path is represented in the left panels of Fig. 13, where it is simply called F. The values of F are indicated by dots. The analogous path F' for nonreactive trajectories is shown in the right panels. The prefactor in Eq. (21) is a decreasing function of k for both reactive and nonreactive paths (see the indigo squares in Figs. 10 to 12; remember that for reactive trajectories, $\overline{\phi}_1^k$ increases as k increases while for nonreactive trajectories,

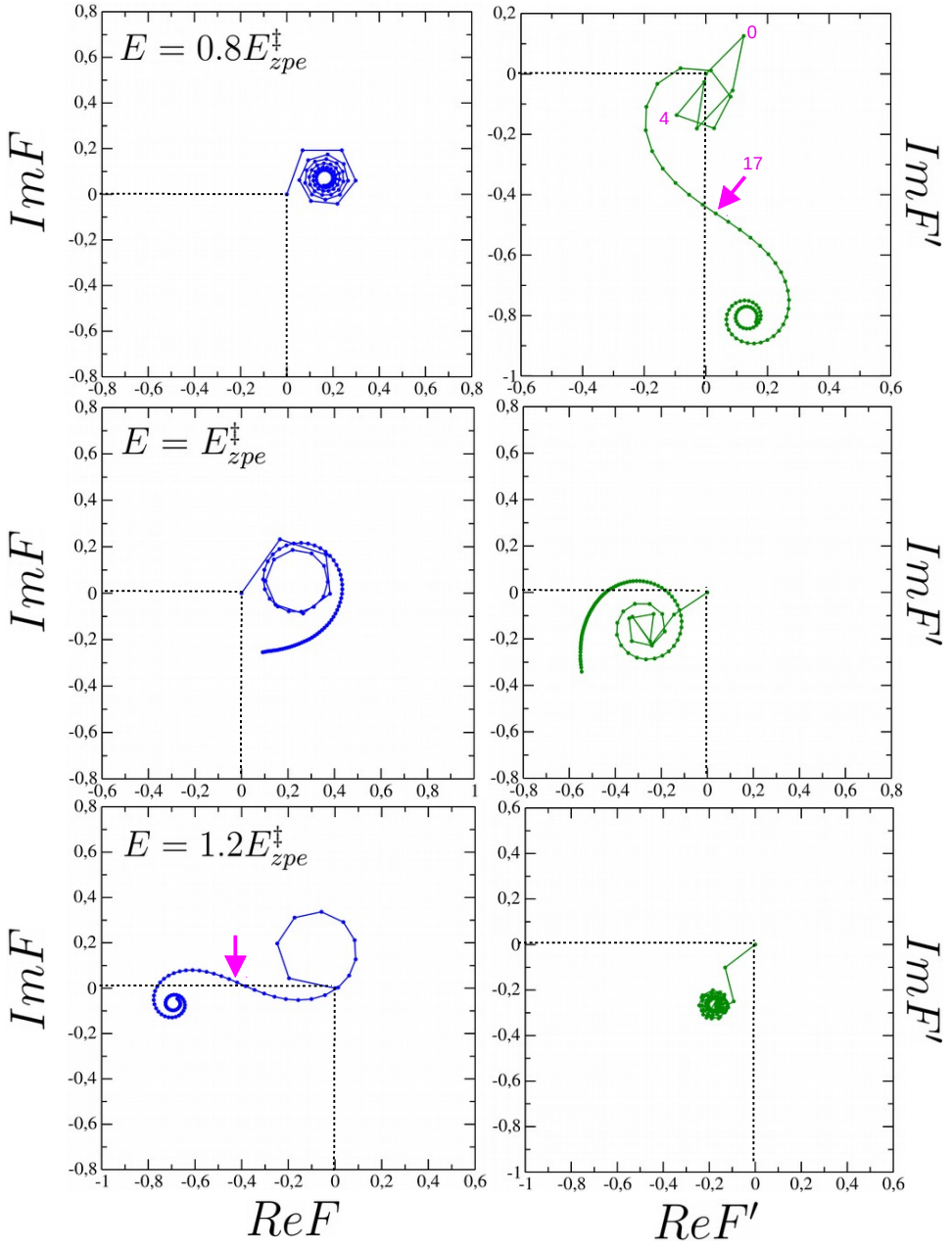

Figure 13: Representation in the complex plane of the CSMT folding functions F and F', based on Eq. (21). $\mu = 19$ amu. See text for more details.

$\overline{\phi}_1^k$ decreases as k increases). Therefore, the length of the segments in Fig. 13 decreases as N increases. At $0.8E^{\ddagger}_{zpe}$ (upper panels in Fig. 13), F forms an *Archimedean spiral* making $|S_{00}(E)|$ very small, while F' forms a *Cornu spiral* making $|S'_{00}(E)|$ large. The Archimedean

spiral is run clockwize as N increases, for two reasons: first, for reactive paths, the phase Ω_N decreases as N increases (see Fig. 10); second, $\Omega_N - \Omega_{N+1}$ turns out to be lower than π. Therefore, the $(N+1)^{th}$ segment in the left upper panel of Fig. 13 is necessarily oriented towards the right with respect to the N^{th} segment. As for the Cornu spiral (right upper panel in Fig. 13), the magenta arrow corresponds to the value of F' obtained when Ω_N is the stationary phase, which is the case at $N = 17$. This phase is located at the head of the magenta arrow in Fig. 10. When N increases from 0 to 17, Ω_N increases (see in Fig. 10 the orange dots from π to the magenta arrow). From $N = 3$ to $N = 17$, $\Omega_{N+1} - \Omega_N$ is lower than π and the Cornu spiral is run counterclockwize. From $N = 17$ on, Ω_N decreases (see in Fig. 10 the orange dots from the magenta arrow to $\overline{\phi}_{po}$), $\Omega_N - \Omega_{N+1}$ is lower than π and the Cornu spiral is then run clockwize. To summarize, below the threshold, F is folded in on itself while F' is unfolded. Moreover, the modulus of F' is mainly due to the set of ~ 25 trajectories roughly centered at $k = 17$ which define the most linear, or less curved part of the Cornu spiral. The folding functions at the threshold are represented in the middle panels of Fig. 13. F and F' are about to unfold and fold, respectively; they are in an intermediate situation that makes them look similar, the main difference being that F is run clockwize while F' is run anticlockwize. Fig. 11 indeed shows that for reactive paths, Ω_N decreases as N increases while for nonreactive paths, the opposite happens. The end of the spirals do not fold in on themselves. They are more and more linear as N takes large values, since the phases converge toward the same value. Dots accumulate at the end of the spirals, since an infinite number of resonant paths contribute to the reactivity. Those are geometrical manifestations of the resonance. At $1.2E^{\ddagger}_{zpe}$ (lower panels in Fig. 13), the scenario is the opposite of that at $0.8E^{\ddagger}_{zpe}$. F forms a Cornu spiral making $|S_{00}(E)|$ large, while F' forms an Archimedean spiral (not visible in Fig. 13) making $|S'_{00}(E)|$ very small. The SCIVR folding functions presented in Appendix C have essentially the same features.

We wish to outline the fact that a threshold resonance is expected at $E^{\ddagger}_{zpe}$ whatever the initial quantum state of the reagents consistent with reaction. The reason is that there

will always be trapped trajectories at the frontier between reactive and nonreactive paths. Consequently, there will necessarily be resonant paths with equal phases right at $E^{\ddagger}_{zpe}$ and, thus, fully constructive interferences enhancing the reactivity.

4.2 Analytical approach of the reactivity threshold

We have found that a resonance occurs at $E^{\ddagger}_{zpe}$, the TS or activated complex ZPE. Moreover, passage through this resonance as the energy increases allows quantum interferences between reactive paths to shift from destructive to constructive and vice versa for nonreactive paths, thereby creating a reactivity threshold at $E^{\ddagger}_{zpe}$. We now come to the last stage of this work, which consists in treating analytically the dynamics of reactive paths. This will allow us not only to clarify some points previously discussed, but also to provide new theoretical arguments sheding light on the quantization of the activated complex or the TS.

4.2.1 Description of the dynamics

For R within the range $[-\Delta/2, \Delta/2]$, we approximate the potential of Fig. 1 by its second order development

$$V(R, \phi) = \frac{1}{2} I \omega^{\ddagger 2} \phi^2. \tag{28}$$

As stated in Sec. 2, this expression is quite accurate around $E^{\ddagger}_{zpe}$. Therefore, the latter is well approximated by $\hbar\omega^{\ddagger}/2$ (for clarity's sake, we stop expressing actions in $\hbar$ unit; $\hbar$ will thus explicitely appear in the developments). Outside the range $[-\Delta/2, \Delta/2]$, $V(R, \phi)$ is taken at 0. We thus have reagent and product half planes separated by a channel of parabolic section and length Δ.

Within the channel, the previous potential involves an infinite number of POs vibrating perpendicular to the R-axis. However, if one adds along this axis an Eckart barrier of infinitesimal height centered at $R = 0$, all these POs disappear but the one at $R = 0$, so the existence of a unique TS is ensured. In the following, we will assume that such a barrier is

present, but we will neglect it in the analytical treatment of the channel crossing.

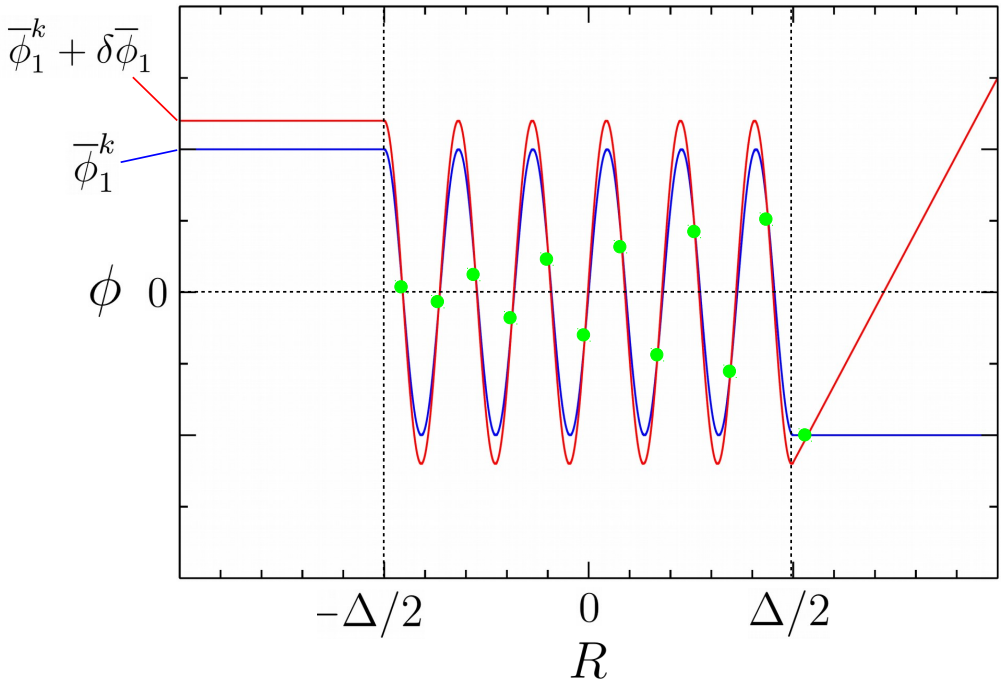

Figure 14: The blue trajectory is an example of path which contributes to $S_{00}(E)$. The crossings between the blue and red paths, represented by the green circles, are called focal points. The Maslov index η is equal to their number in the limit where $\delta\overline{\phi}_1^k$ tends to 0 ($\eta = 12$ in the present case). See text for more details.

As in Sec. 4.1, we use Eqs. (21) and (22), built from the trajectories starting from the reagents with $P_1 = \sqrt{2\mu E}$, $J_1 = 0$, $\overline{\phi}_1^k$ and ending in the products with $J_2 = 0$. We now determine analytically the expression of the $\overline{\phi}_1^k$'s. We ignore the case $k = 0$ as the corresponding trajectory plays a minor role in the following. For $k > 0$, the previous trajectories typically resemble the blue path in Fig. 14. This path comes from the reagents parallel to the R-axis. At the entrance of the parabolic channel, the kinetic energy $\frac{P^2}{2\mu}$ suddenly decreases from E to $\left(E - \frac{1}{2} I \omega^{\ddagger 2} \overline{\phi}_1^{k\,2}\right)$ [see Eqs. (3) and (28), with $H = E$ and $J = J_1 = 0$]. Consequently, P suddenly reduces to the value

$$P_k = \left[2\mu \left(E - \frac{1}{2} I \omega^{\ddagger 2} \overline{\phi}_1^{k\,2}\right)\right]^{1/2} \tag{29}$$

and remains constant up to the exit of the channel. Within the latter, and thus at the TS, the rigid diatom oscillates with the vibrational energy

$$E_{vk}^{\ddagger} = \frac{1}{2} I \omega^{\ddagger 2} \overline{\phi}_1^{k\,2}. \tag{30}$$

The period of time T spent by the blue trajectory within the channel is equal to an integer number l of half vibrational periods $\frac{\pi}{\omega^{\ddagger}}$ ($l = 11$ in Fig. 14). Then, the trajectory leaves the parabolic channel with $J_2 = 0$, while P takes its initial value back. From the exit of the channel on, the trajectory is parallel to the R-axis. Within the channel, the time dependences of ϕ and J are given by

$$\phi(\tau) = \overline{\phi}_1 cos(\omega^{\ddagger} \tau) \tag{31}$$

and

$$J(\tau) = I\dot{\phi} = -I\omega^{\ddagger}\overline{\phi}_1 sin(\omega^{\ddagger}\tau), \tag{32}$$

where τ is 0 at $R = -\Delta/2$. Moreover, the channel crossing time is

$$T = \frac{\mu \Delta}{P}. \tag{33}$$

However, we have just seen that

$$T = \frac{l\pi}{\omega^{\ddagger}} \tag{34}$$

where l is an integer, and we immediately see that substituting the right-hand-side of Eq. (34) to τ in Eq. (32) implies $J(T) = 0$, as it should be. Note from Eq. (32) that there is no analytical solution of the equation $J(T) = J_2$ if the latter is different from 0. Substituting the right-hand-side of Eq. (29) for P in Eq. (33) and equating the resulting expression to the right-hand-side of Eq. (34) gives

$$\overline{\phi}_1^{k} = \left[\frac{2E}{I\omega^{\ddagger 2}} - \frac{\mu \Delta^2}{I\pi^2 l^2} \right]^{1/2}. \tag{35}$$

Since the term under the square root must be positive, we necessarily have

$$l \geq \left[\frac{\mu\Delta^2\omega^{\ddagger 2}}{2\pi^2 E}\right]^{1/2} \tag{36}$$

and, thus,

$$l > l_0 = int\left(\left[\frac{\mu\Delta^2\omega^{\ddagger 2}}{2\pi^2 E}\right]^{1/2}\right) \tag{37}$$

where $int(x)$ means integer part of x. Replacing l by $l_0 + k$ in Eq. (35), we have

$$\overline{\phi}_1^k = \left[\frac{2E}{I\omega^{\ddagger 2}} - \frac{\mu\Delta^2}{I\pi^2(l_0+k)^2}\right]^{1/2}. \tag{38}$$

$\overline{\phi}_{po}$, obtained by making k tend to $+\infty$ in the above expression, results in $\sqrt{\frac{2E}{I}}/\omega^{\ddagger}$. In Eq. (21), each term of the sum involves the phase $\Psi_k = \Omega_k/\hbar - \pi\eta_k/2 + \pi/4$ with $\Omega_k = \Omega_{Pk} + \Omega_{Jk}$. Using Eq. (24) with $R_1 = -\Delta/2$, $R_2 = \Delta/2$, $P_1 = \sqrt{2\mu E} = P_2$, the fact that $P = P_k$ between R_1 and R_2, and Eq. (29), we obtain

$$\Omega_{Pk} = \frac{\mu\omega^{\ddagger}\Delta^2}{\pi(l_0+k)} - \Delta\sqrt{2\mu E}. \tag{39}$$

Moreover, Ω_{Jk} is given by $l_0 + k$ times half the area of the ellipse in the (ϕ, J) plane defined by

$$\frac{J^2}{2I} + \frac{1}{2}I\omega^{\ddagger 2}\phi^2 = \frac{1}{2}I\omega^{\ddagger 2}\overline{\phi}_1^{k\,2}. \tag{40}$$

After some steps of algebra and using Eq. (38), we find

$$\Omega_{Jk} = \frac{\pi E}{\omega^{\ddagger}}(l_0+k) - \frac{\mu\omega^{\ddagger}\Delta^2}{2\pi(l_0+k)}. \tag{41}$$

The Maslov index η_k is accurately calculated as follows. The blue trajectory in Fig. 14 starts from $(R_\infty, \overline{\phi}_1^k)$ where R_∞ tends to $-\infty$. Its energy is E and its initial direction is parallel to the R-axis. Therefore, this path arrives at R_1 with $\overline{\phi}_1^k$. The red trajectory in Fig. 14 also

starts from $(R_\infty, \overline{\phi}_1^k)$ with E. However, its initial direction makes a positive infinitesimal angle with the R-axis. Therefore, the red path arrives at R_1 with $\overline{\phi}_1^k + \delta\overline{\phi}_1$ where $\delta\overline{\phi}_1$ is positive and infinitesimal. The latter is obviously exaggerated in Fig. 14 for clarity's sake. We can now define η_k: this is the number of crossings between the blue and red paths. These crossings, or focal points, are represented in Fig. 14 by the green dots. In fact, the velocity along the R-axis is slightly lower for the red path than for the blue path since both are at the same energy but $V(R_1, \overline{\phi}_1^k + \delta\overline{\phi}_1)$ is slightly larger than $V(R_1, \overline{\phi}_1^k)$. This is the reason why the green dots are all the more distant from the reaction path (horizontal dashed line) as they are close to the exit of the channel. However, if we make $\delta\overline{\phi}_1$ tends to 0, as it should be, it is clear that the green dots inside the channel will move inward to eventually be aligned on the reaction path. In addition, the right most green dot located outside the channel will be sent to infinity. Therefore, η_k is equal to the number of green dots inside the channel, i.e., the number $l_0 + k$ of half vibrational periods performed within the channel, plus one unit:

$$\eta_k = l_0 + k + 1. \tag{42}$$

This justifies our definition of η_k in Sec. 4.1.2 (in fact, we used $\eta_k = l_0 + k$ and applied it to resonant paths. However, for these trajectories, $l_0 + k$ is very large, so the last unit in Eq. (42) can be neglected).

4.2.2 Analysis of the Phase

From Eqs. (39), (41) and (42), $\Psi_k/\hbar = \Omega_{Pk}/\hbar + \Omega_{Jk}/\hbar - \pi\eta_k/2 + \pi/4$ reads

$$\frac{\Psi_k}{\hbar} = \frac{\mu\omega^\ddagger\Delta^2}{2\pi\hbar(l_0+k)} + \frac{\pi(l_0+k)}{\hbar\omega^\ddagger}\left(E - \frac{\hbar\omega^\ddagger}{2}\right) - \Delta\sqrt{2\mu E}/\hbar - \pi/4. \tag{43}$$

As seen in Sec. 4.1, the resonance is mostly due to the infinite set of trajectories trapped a long period of time in the vicinity of the PO. For these resonant paths, corresponding to large values of k, $\Psi_k/\hbar$ reduces to the last three terms of Eq. (43), since the first one tends to

0. The last two terms do not depend on k. The second term accounts for two inverse effects when k increases by 1 unit: since the $(k+1)^{th}$ trajectory spends a half vibrational period more than the k^{th} trajectory within the channel, the vibrational action increases by $\pi E/\omega^{\ddagger}$ while the increase of the Maslov index removes $\hbar\pi/2$ from the previous increase. Eq. (43) shows that these two effects exactly offset each other whenever $E = \hbar\omega^{\ddagger}/2 = E^{\ddagger}_{zpe}$. The consequence of this compensation is that right at the threshold and for the large values of k, $\Psi_k/\hbar$ reduces to the constant value $(\pi/4 - \Delta\sqrt{2\mu E})$ [see Eq. (43)]. In other words, the Ψ_k's match for an infinite number of terms, thus, leading to a resonance. Out of the resonance, but still for the large k's, the difference between two consecutive $\Psi_k/\hbar$'s is $(\pi E/\omega^{\ddagger} - \hbar\pi/2)$, independent on k. The sign of this difference defines the orientation of the phase peak.

One may invert Eq. (38) in order to express $l_0 + k$ in terms of $\overline{\phi}_1^k$ and substitute $l_0 + k$ with the resulting expression in Eq. (43). The final result is

$$\frac{\Psi_k}{\hbar} = \sqrt{\frac{\mu}{2}}\frac{\Delta}{\hbar}\left[\sqrt{\left(E - \frac{1}{2}I\omega^{\ddagger 2}\overline{\phi}_1^{k\,2}\right)} + \frac{\left(E - \frac{\hbar\omega^{\ddagger}}{2}\right)}{\sqrt{\left(E - \frac{1}{2}I\omega^{\ddagger 2}\overline{\phi}_1^{k\,2}\right)}}\right] - \Delta\sqrt{2\mu E}/\hbar - \pi/4, \qquad (44)$$

or equivalently,

$$\frac{\Psi_k}{\hbar} = \frac{\sqrt{\mu I}\Delta\omega^{\ddagger}}{2\hbar}\left[\sqrt{\left(\overline{\phi}_{po}^{2} - \overline{\phi}_1^{k\,2}\right)} + \frac{\left(\overline{\phi}_{po}^{2} - \overline{\phi}_{po}^{zpe\,2}\right)}{\sqrt{\left(\overline{\phi}_{po}^{2} - \overline{\phi}_1^{k\,2}\right)}}\right] - \Delta\sqrt{2\mu E}/\hbar - \pi/4. \qquad (45)$$

In Eq. (45), $\overline{\phi}_{po} = \sqrt{\frac{2E}{I}}/\omega^{\ddagger}$ [see right after Eq. (38)], and $\overline{\phi}_{po}^{zpe}$ is the value of $\overline{\phi}_{po}$ at the threshold. In these expressions, the change in orientation of the phase peak at the energy threshold appears very clearly, as well as the fact that the peak is centered at $\overline{\phi}_{po}$. In Fig. 15, the values of $\frac{\Psi_k}{\hbar}$ obtained by using the above expressions are shown at $E = 0.8E^{\ddagger}_{zpe}$ (circles), $E = E^{\ddagger}_{zpe}$ (squares) and $E = 1.2E^{\ddagger}_{zpe}$ (diamonds). Qualitatively, the basic features of the

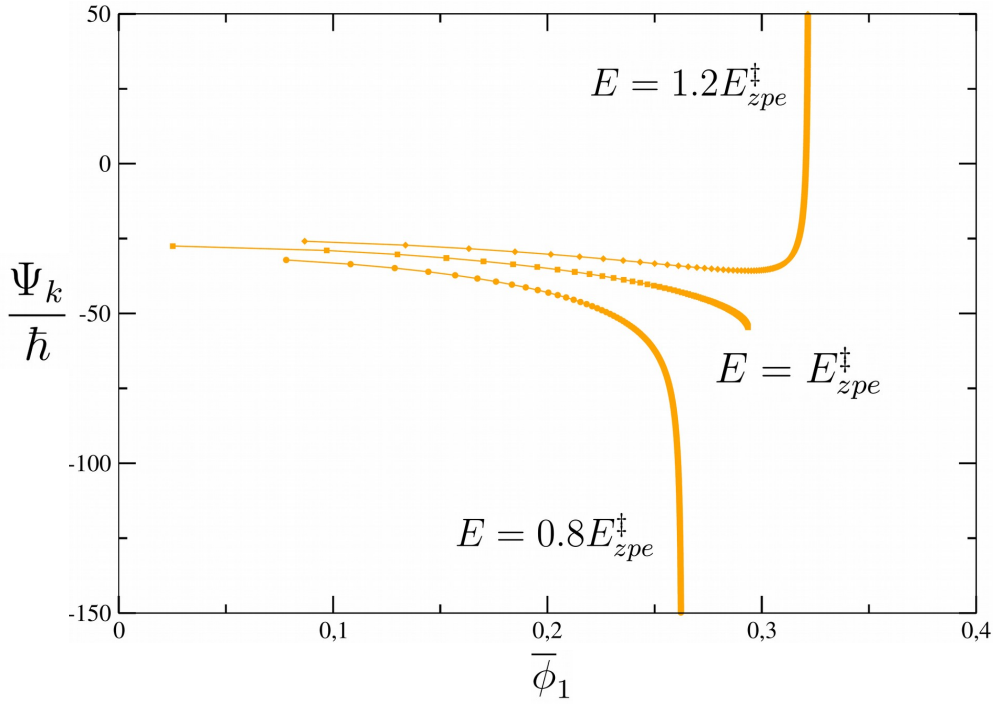

Figure 15: Representation, for the parabolic channel model, of the phase $\frac{\Psi_k}{\hbar}$ assigned to the trajectories contributing to $S_{00}(E)$. These phases, given by Eqs. (43)-(45), are shown for the three energies indicated in the drawing. $\mu = 19$ amu. The symbols corresponding to $k = 0$ are not drawn.

phases represented in Figs. 10 to 12 are well reproduced (focus on the reactive side of $\overline{\phi}_{po}$). The peak is down (up) below (above) the threshold, and at the threshold, the phase is given by the right upper quarter of an ellipse corresponding to the first term within the square brackets of Eqs. (44) and (45). The right most part of the ellipse, tangent to the vertical line defined by $\overline{\phi}_1^k = \overline{\phi}_{po}$, supports our previous assumption that the orange circles in Fig. 11, scattered over a dozen units along the dotted line, have inaccurate positions due to numerical instabilities and should instead form a continuous line.

Our analysis would have been more complete if we could have extended the previous developments to nonreactive trajectories. However, their dynamics are more complex and we have not found a way to simply describe them.

4.2.3 Quantization of the activated complex

The CSMT F-folding function is represented in Fig. 16 from $k = 3$ on for $E = 1.2E^{\ddagger}_{zpe}$ and $\mu = 19$ amu. A few values of k are indicated in order to show the direction of travel of the folding function (as CSMT lacks accuracy for the smallest values of k, we determined the folding function from SCIVR up to the angle between $\overline{\phi}^2_1$ and $\overline{\phi}^3_1$ where the phase index $\bar{\nu}$ jumps, and then switched to CSMT). The folding function is a Cornu spiral, run clockwize from the origin to $k = 24$ (green square in Fig. 16), counterclockwize beyond. The length of the dashed segment is equal to the modulus of $S_{00}(E)$, and the dotted segment going from $k = 17$ to $k = 33$ has the same length as the dashed segment. The spiral has the same shape as its analog in Figs. 13 (lower left panel). However, it is oriented differently since the present potential [Eq. (28)] is different from the previously used one [Eq. (2)].

The phase $\Psi_k/\hbar$ and the vibrational energy $E^{\ddagger}_{vk}$ at the TS are shown in Fig. 17. The latter is given in unit of $E^{\ddagger}_{zpe}$. The same symbol colors as in Fig. 16 are used for the same values of k. The phase is stationary at $k = 24$ (green square in Fig. 17; $\Psi_k/\hbar$ is not equal to 2 at this point; we just shifted it for the clarity of the figure, which has no consequence on the reasoning). The fact that the phase decreases (increases) before (after) $k = 24$ is consistent with the clockwize (anticlockwize) run of the Cornu spiral before (after) $k = 24$.

The value of $|S_{00}(E)|$ is mainly due to the trajectories corresponding to the blue squares numbered from 17 to 33 (we will call these paths the "blue trajectories" further on). The dotted segment in Fig. 16 has indeed the same length has the dashed one, equal to $|S_{00}(E)|$, thus implying that the combined action of all the red circles in Fig. 16 just rotates (and slightly translates) the contribution of the blue squares to $S_{00}(E)$ without changing its modulus. Besides, the TS vibrational energies for the blue trajectories are seen in Fig. 17 to be distributed closely around $E^{\ddagger}_{v24}$, which turns out to be equal to $E^{\ddagger}_{zpe}$ (this is analytically justified further below). Therefore, those trajectories mostly contributing to the reactivity – the blue trajectories – cross the TS with a vibrational energy close to $E^{\ddagger}_{zpe}$ and an average vibrational energy very close to $E^{\ddagger}_{zpe}$. This remarkable result, which we confirmed

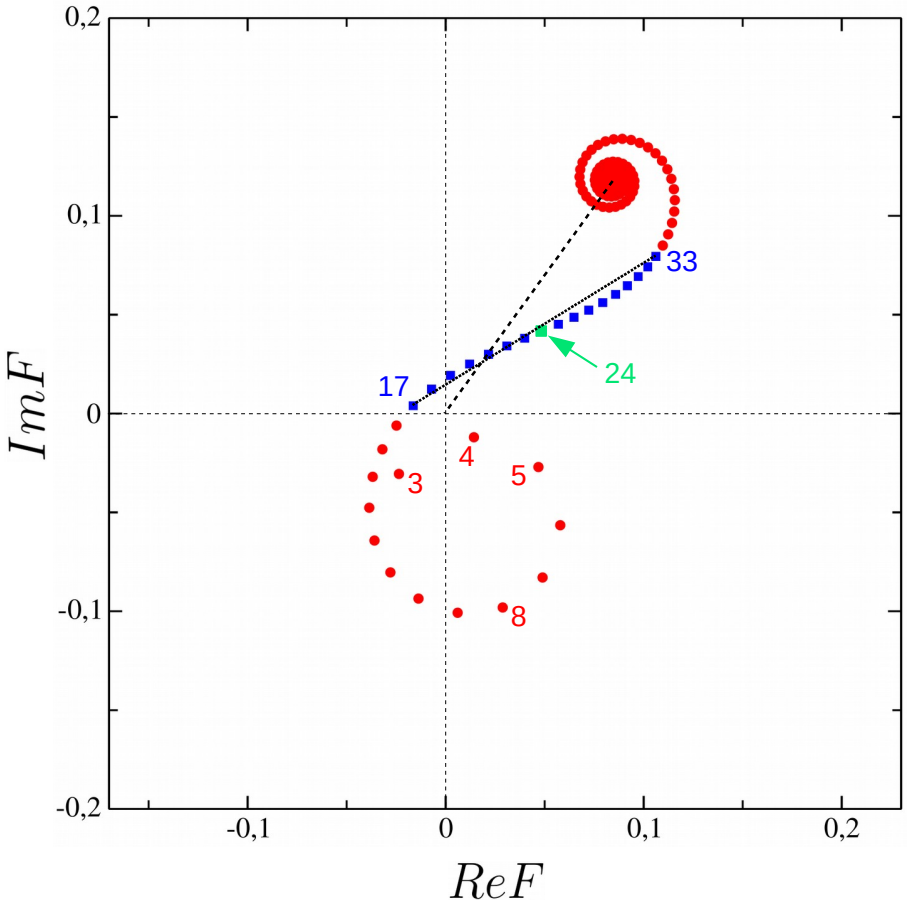

Figure 16: CSMT F-folding function represented from $k = 3$ on. $E = 1.2E^{\ddagger}_{zpe}$ and $\mu = 19$ amu. $|S_{00}(E)|$ is equal to the length of the dashed segment, also equal to that of the dotted segment whose extremities are the blue squares numbered 17 and 33. The green square numbered 24 corresponds to the stationary phase (see Fig. 17).

for several energies above the threshold, strongly supports the idea of quantized transition state.[13,56] In addition to that, nearly half of the previous trajectories cross the TS with a vibrational energy lower than $E^{\ddagger}_{zpe}$ (see trajectories 17 to 23 in Fig. 17). This challenges the fairly widespread idea in the QCTM community that the vibrational energy of the activated complex must be greater than or equal to its ZPE.

We now prove that the vibrational energy at the TS for the trajectory making the phase stationary, call it $E^{\ddagger}_{vsp}$, is equal to $E^{\ddagger}_{zpe}$. It is clear from Fig. 17 that we will not make a significant error if we consider k as a continuous variable while estimating the stationary

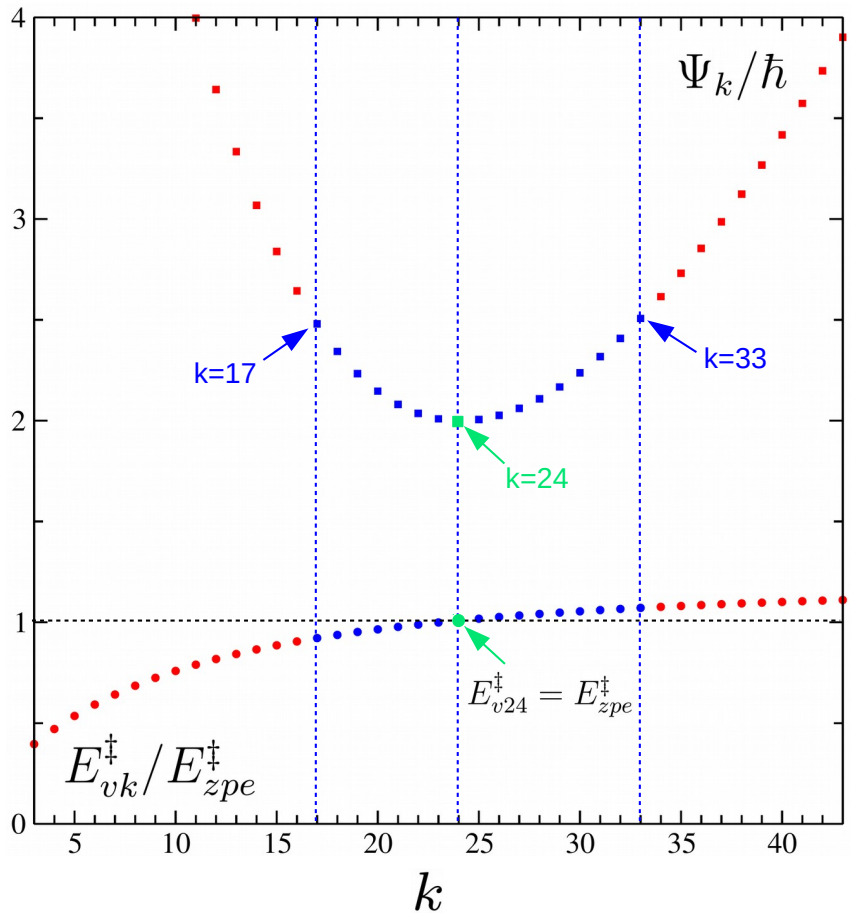

Figure 17: The phase $\Psi_k/\hbar$ and the vibrational energy $E^{\ddagger}_{vk}$ at the TS (in unit of $E^{\ddagger}_{zpe}$) are shown for k between 3 and 43. $E = 1.2E^{\ddagger}_{zpe}$ and $\mu = 19$ amu. The choice of the colors in terms of k is as in Fig. 16.

value of Ψ_k. Within this approximation, the value of k making Ψ_k stationary is found from Eq. (43) to be solution of

$$\frac{d\Psi_k}{dk} = -\frac{\mu\omega^{\ddagger}\Delta^2}{2\pi(l_0+k)^2} + \frac{\pi}{\omega^{\ddagger}}\left(E - \frac{\hbar\omega^{\ddagger}}{2}\right) = 0. \tag{46}$$

$E^{\ddagger}_{vsp}$ is then found by deducing the expression of $(l_0+k)^{-2}$ from Eq. (46), introducing this expression in Eq. (38), and using Eq. (30). The final result is as expected:

$$E^{\ddagger}_{vsp} = \frac{\hbar\omega^{\ddagger}}{2} = E^{\ddagger}_{zpe}. \tag{47}$$

Moreover, it is seen in Fig. 18 that this relation is accurately satisfied for the potential of Fig. 1. To sum up, $S_{00}(E)$ is mainly due to the blue trajectories whose initial conditions are

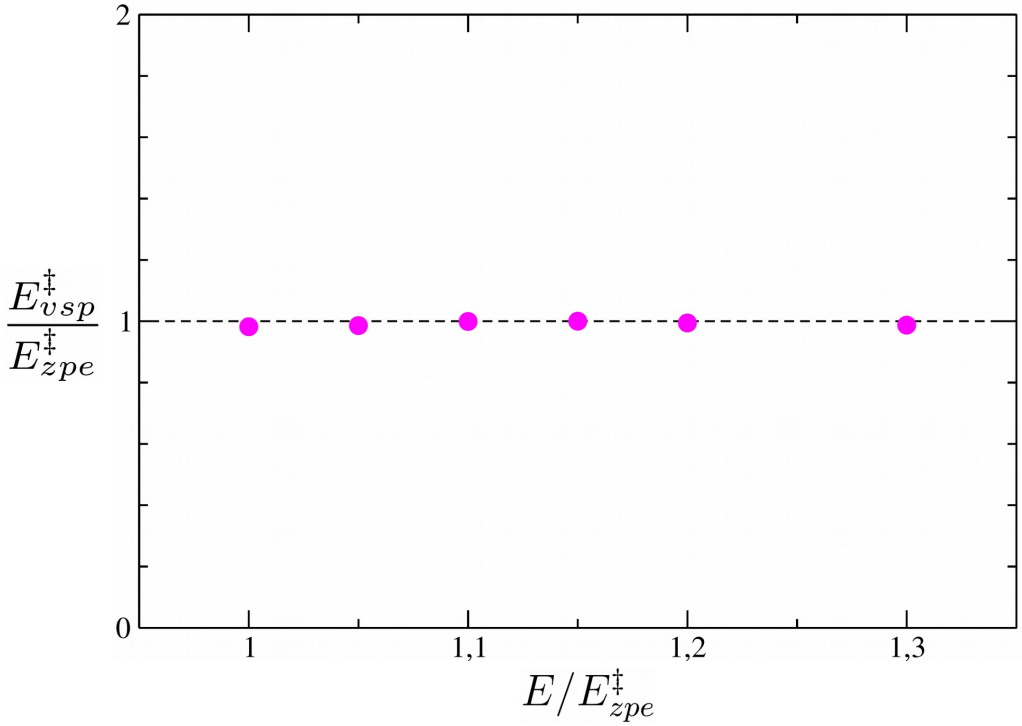

Figure 18: $E^{\ddagger}_{vsp}/E^{\ddagger}_{zpe}$ in terms of $E/E^{\ddagger}_{zpe}$ for the potential of Fig. 1. $\mu = 19$ amu. The dots correspond to $E/E^{\ddagger}_{zpe} = 1.01, 1.05, 1.1, 1.15, 1.2$ and 1.3. For each energy, the trajectory making the phase stationary was sought, and $E^{\ddagger}_{vsp}$ is the vibrational energy obtained at the moment when the trajectory crosses the transition state.

close to the one making the phase $\Psi_k/\hbar$ stationary, the vibrational energies at the TS are closely distributed around $E^{\ddagger}_{zpe}$, and their average value is nearly equal to $E^{\ddagger}_{zpe}$.

Now, what about below the threshold ? We know that the phase monotonously decreases with $\overline{\phi}^k_1$ [see Fig. 10 (reactive paths) and the curve in Fig. 15 corresponding to $E = 0.8E^{\ddagger}_{zpe}$]. For reactive paths, however, k increases with $\overline{\phi}^k_1$ [see Eq. (38)] so the phase monotonously decreases also with k. There is thus no stationary phase so that when we calculate $|S_{00}(E)|$ using Eq. (21), the different terms of the sum interfere in a destructive way. As a consequence, the folding function takes the shape of an Archimedean spiral folded in on itself, thus explaining the smallness of $|S_{00}(E)|$ (see the left upper panel of Fig. 13). However, if we stick

to these qualitative considerations, we do not see which trajectories can contribute the most to $|S_{00}(E)|$ (when the latter is not too small), nor what their vibrational energies can be at the TS. To find out more, we can approximately solve Eq. (21) by transforming its sum into an integral and applying the saddle point method which involves an appropriate deformation of the integration contour in the complex plane.[23,29,57] Using Eqs. (43) and (B.1), Eq. (21) then becomes

$$S_{00}(E) = \int_C g(z) e^{\frac{f(z)}{\hbar}} dz \tag{48}$$

where the contour C is defined further below,

$$z = l_0 + k \tag{49}$$

along the real axis,

$$f(z) = i \left[\frac{\mu \omega^{\ddagger} \Delta^2}{2\pi z} + \frac{\pi}{\omega^{\ddagger}} \left(E - \frac{\hbar \omega^{\ddagger}}{2} \right) z \right] \tag{50}$$

and

$$g(z) = i \left[\frac{\pi \hbar}{2} \left| \frac{2I\pi^3 z^3}{\mu \omega^{\ddagger} \Delta^2} \left[E - \frac{\mu \omega^{\ddagger 2} \Delta^2}{2\pi^2 z^2} \right]^{1/2} \right| \right]^{-1/2} e^{-i\left(\Delta\sqrt{2\mu E}/\hbar + \pi/4\right)}. \tag{51}$$

In the limit where $\hbar$ tends to 0, the saddle point method[57] tells us that

$$S_{00}(E) = \sqrt{\frac{2\pi\hbar}{|f''(z_0)|}}\, g(z_0) e^{\frac{f(z_0)}{\hbar}} e^{i\alpha} \tag{52}$$

where

$$f'(z_0) = 0 \tag{53}$$

and

$$\alpha = \pi/2 - arg[f''(z_0)]/2 \tag{54}$$

[note that this angle has nothing to do with α in Eq. (2)]. z_0 locates the saddle point of $|f(z)|^2$ while α gives the orientation of the steepest descent path with respect to the real

axis in the neighborhood of z_0. The contour C must be distorted from the real axis so as to coincide with the steepest descent path in the vicinity of z_0 and be run in the direction given by $e^{i\alpha}$. Note that the present developments involve two approximations: the first is the passage from a sum [Eq. (21)] to an integral [Eq. (48)], and the second is Eq. (52), accurate only if $\hbar$ takes negligible values compared to the actions into play in the process, which is not really the case for the vibrational action (E is indeed lower than $E^{\ddagger}_{zpe}$). The expressions we are going to establish will therefore help us to rationalize the dynamics rather than to describe them precisely. After a few steps of algebra, one finds that the solution of Eq. (53) is

$$z_0 = -i \left[\frac{\mu {\omega^{\ddagger}}^2 \Delta^2}{\pi^2 (\hbar \omega^{\ddagger} - 2E)} \right]^{1/2} \tag{55}$$

(the opposite of the right-hand-side of Eq. (55) is also a solution of Eq. (53) ; it is however not physically acceptable, as shown a few lines further on). Moreover,

$$f''(z_0) = \frac{\pi^2 (\hbar \omega^{\ddagger} - 2E)^{3/2}}{\mu^{1/2} {\omega^{\ddagger}}^2 \Delta}. \tag{56}$$

$f''(z_0)$ is thus positive real, so α equals $\pi/2$ [see Eq. (52)]. Therefore, in the neighborhood of z_0, the contour C runs upward along the imaginary axis. Setting $z = iy$, we can rewrite Eq. (48) as

$$S_{00}(E) = \int_{-\infty}^{0} ig(iy) e^{\frac{f(iy)}{\hbar}} dy. \tag{57}$$

The exponential term $e^{\frac{f(iy)}{\hbar}}$ of the integrand is represented in Fig. 19 by the blue bell curve with red ends (this curve involves exponential damping; if we had used the other solution of Eq. (53), i.e., $-z_0$ instead of z_0, we would have obtained exponential enhancement instead of damping and $|S_{00}(E)|$ would have been infinite). E was taken at $0.95 E^{\ddagger}_{zpe}$ and μ at 19. The top of this curve corresponds to $y_0 = z_0/i$. The statistical weight of the y value is proportional to the squared modulus of the integrand of Eq. (57). This weight is proportional to $e^{2\frac{f(iy)}{\hbar}}$, represented by the green curve in Fig. 19 (for clarity's sake, the two previous curves were

rescaled so as to be equal to 2 at their maximum). The green curve shows that the values of y that contribute to $S_{00}(E)$ belong approximately to the range [-160,-40], for outside this range, the statistical weight is negligible. The term $e^{\frac{f(iy)}{\hbar}}$ is represented in blue within the previous range, in red outside. This choice of colors is identical to that in Fig. 17 where the blue color emphasizes the real values of k which contribute the most to $S_{00}(E)$. In both cases (Figs. 17 and 19), the relevant initial conditions (k and y) are distributed around the values that make stationary the arguments of the exponential terms ($i\frac{\Psi_k}{\hbar}$ and $\frac{f(iy)}{\hbar}$).

The vibrational energy of the activated complex, obtained by replacing $l_0 + k$ by iy in Eqs. (30) and (38), is

$$E_v^\ddagger(y) = E + \frac{\mu {\omega^\ddagger}^2 \Delta^2}{2I\pi^2 y^2}. \tag{58}$$

This energy is thus larger than the total energy, thus implying that the kinetic energy is negative within the channel. This can be explained from the fact that the channel crossing time has the pure imaginary value

$$T(y) = \frac{iy\pi}{\omega^\ddagger}. \tag{59}$$

This time is deduced from Eq. (34), the fact that l was renamed $l_0 + k$ right after Eq. (37), then z in Eq. (49) and finally, iy along the steepest descent path in the vicinity of the saddle point. In this description, R keeps real while P, proportional to the ratio of a real distance and a pure imaginary time, is pure imaginary. This explains why the kinetic energy is negative within the channel.[58] $E_v^\ddagger(y)$ is represented in unit of $E_{zpe}^\ddagger$ in Fig. 19. Substituting $y_0 = z_0/i$ for y in Eq. (58) and using Eq. (55) shows that the vibrational energy is equal to $E_{zpe}^\ddagger$ at the stationary value of $f(iy)$. We also note that the most probable values of $E_v^\ddagger(y)$, represented in blue, are closely distributed around $E_{zpe}^\ddagger$, and their average value is nearly equal to $E_{zpe}^\ddagger$. The situations below and above the threshold are thus very similar. In both cases, the activated complex appears to be quantized. Finally, Eqs. (50)-(52), (55) and (56)

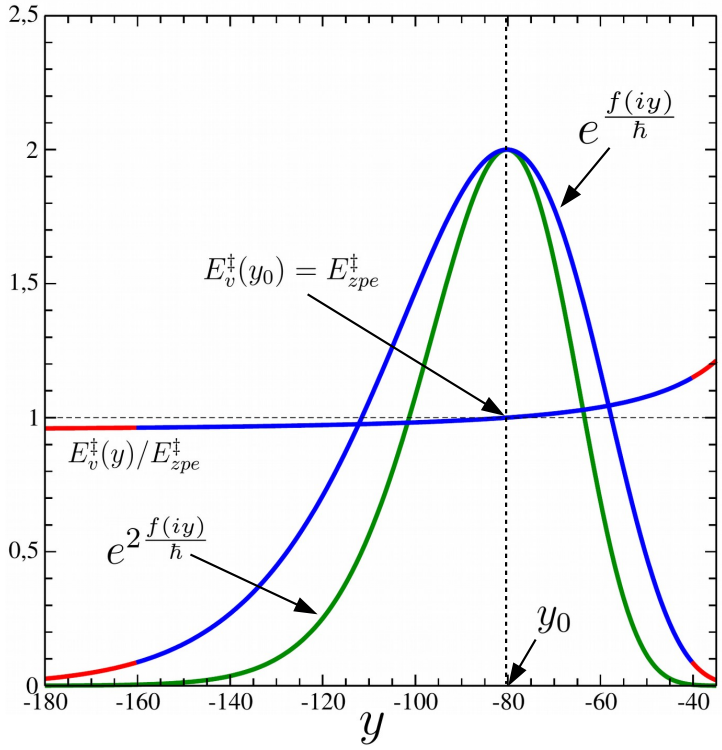

Figure 19: Representation of $e^{\frac{f(iy)}{\hbar}}$, its square value, and the ratio $E_v^{\ddagger}(y)/E_{zpe}^{\ddagger}$. $E = 0.95E_{zpe}^{\ddagger}$ and $\mu = 19$ amu. As in Figs. 16 and 17, the blue color emphasizes the range of values of y that mainly contribute to $S_{00}(E)$ [see Eq. (57)].

lead after some steps of algebra to the state-to-state probability

$$P_{00}(E) = |S_{00}(E)|^2 = \frac{4\hbar}{\pi^2 I\omega^{\ddagger}} e^{-2\Delta\sqrt{\mu(\hbar\omega^{\ddagger}-2E)}/\hbar}. \tag{60}$$

In fact, above the threshold, it turns out that $P_{00}(E)$ is equal to the pre-exponential factor of Eq. (60), i.e., $4\hbar/(\pi^2 I\omega^{\ddagger})$. This can be shown by transforming Eq. (21) into an integral and solving the latter within the stationary phase approximation.[27,51] Below the threshold, however, $4\hbar/(\pi^2 I\omega^{\ddagger})$ is multiplied by $exp[-2\Delta\sqrt{\mu(\hbar\omega^{\ddagger}-2E)}/\hbar]$, which we recognize as the WKB probability of tunneling through the adiabatic barrier.

4.2.4 Time-energy uncertainty

We consider the standard deviations $\Delta E_v^\ddagger$ and $\Delta T^\ddagger$ of the activated complex vibrational energies and lifetimes at $E = 1.2E_{zpe}^\ddagger$. Since $S_{00}(E)$ is mainly due to the blue trajectories defined by $k = 17, ..., 33$ (see the blue squares in Figs. 16 and 17), $\Delta E_v^\ddagger$ is given by

$$\Delta E_v^\ddagger = \sqrt{\overline{E_v^{\ddagger 2}} - \overline{E_v^\ddagger}^2} \tag{61}$$

with

$$\overline{E_v^{\ddagger 2}} = \frac{\sum_{k=17}^{k=33} p_k {E_{vk}^\ddagger}^2}{\sum_{k=17}^{k=33} p_k} \tag{62}$$

and

$$\overline{E_v^\ddagger} = \frac{\sum_{k=17}^{k=33} p_k E_{vk}^\ddagger}{\sum_{k=17}^{k=33} p_k}, \tag{63}$$

where

$$p_k = \left[\frac{\pi}{2} \left| \frac{\partial J_2}{\partial \overline{\phi}_1} \right|_k \right]^{-1} \tag{64}$$

is the classical statistical weight of the k^{th} trajectory [see Eq. (21) and the lines following Eq. (20)]. $\Delta T^\ddagger$ is given by similar expressions where T_k is substituted for $E_{vk}^\ddagger$. $E_{vk}^\ddagger$ and $T_k^\ddagger$ are given by Eq. (30) and Eq. (34) with $l = l_0 + k$. p_k is straighforwardly deduced from Eq. (B.1). T_k, the activated complex lifetime is here the channel crossing time, but more generally, T_k will be the time to cross the vibrationally adiabatic region encompassing any TS.[33] In Fig. 1, this region is the central band labeled VA. By identifying $\Delta E_v^\ddagger$ and $\Delta T^\ddagger$ with the uncertainties on the activated complex vibrational energy and lifetime, we calculated their product and found $0.37\hbar$. We repeated this calculation for $E/E_{zpe}^\ddagger = 1.005$, 1.02, 1.05 and 1.1 and found, respectively, $0.41\hbar$, $1.00\hbar$, $0.43\hbar$ and $0.87\hbar$. This is again a remarkable result strengthening the notion of quantized activated complex or transition state, and showing that the time-energy uncertainty principle is properly built into classical S-matrix theory. Obviously, saying that the activated complex is quantized does not imply that its vibrational energy is strictly quantized, since we have just seen that the activated

complex is in general in a time-dependent quantum state. Its vibrational energy will be strictly quantized only in the limit where $\Delta T^{\ddagger}$ tends to infinity (see further below).

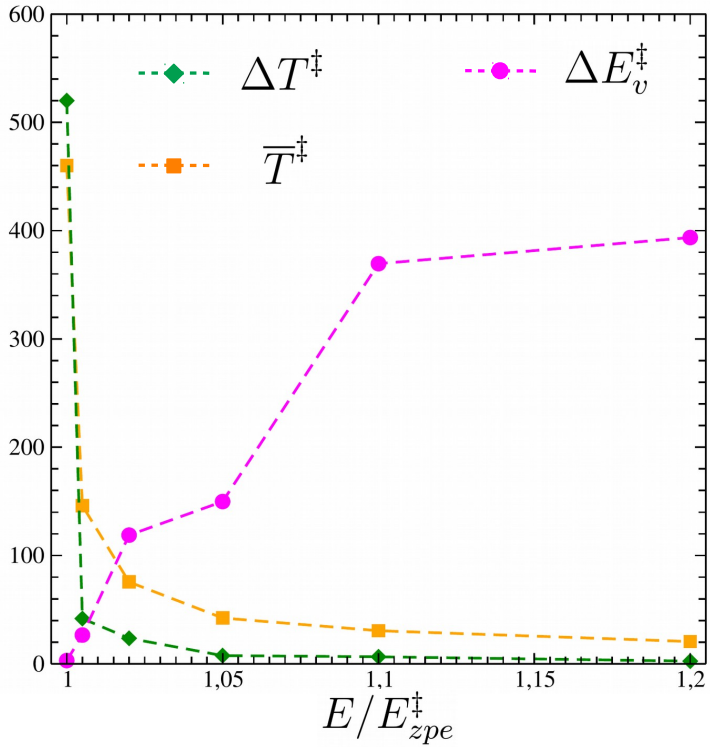

Figure 20: Standard deviation $\Delta E_v^{\ddagger}$, activated complex lifetime $\overline{T}^{\ddagger}$ and standard deviation $\Delta T^{\ddagger}$ represented in terms of $E/E_{zpe}^{\ddagger}$. $\Delta E_v^{\ddagger}$ is given in cm^{-1} while $\overline{T}^{\ddagger}$ and $\Delta T^{\ddagger}$ are expressed in unit of vibrational period along the periodic orbit (23.66 fs). Calculations have been made using Eq. (38), i.e., the harmonic approximation of the potential of Fig. 1. μ was taken at 19 amu. The symbols correspond to $E/E_{zpe}^{\ddagger} = 1$, 1.005, 1.02, 1.05, 1.1 and 1.2. The dashed lines are guides for the eyes.

In Fig. 20, $\Delta T^{\ddagger}$, $\overline{T}^{\ddagger}$ and $\Delta E_v^{\ddagger}$ are represented in terms of $E/E_{zpe}^{\ddagger}$. $\Delta E_v^{\ddagger}$ is given in cm^{-1} while $\Delta T^{\ddagger}$ and $\overline{T}^{\ddagger}$ are expressed in unit of vibrational period along the PO (23.66 fs). For $E/E_{zpe}^{\ddagger} = 1$, the calculations have been performed as follows. Since $E = \hbar\omega/2$, the k-dependent part of $\Psi_k/\hbar$ reduces to the first term of the right-hand-side of Eq. (43), which tends to 0 as k increases. The large values of k define the resonant paths whose phases are all equal. As we have seen before, these paths mainly contribute to $S_{00}(E_{zpe}^{\ddagger})$. We have found that limiting the sum in Eq. (21) to the resonant paths defined by $k \geq 466$ allows us

to reproduce the value of $|S_{00}(E^{\ddagger}_{zpe})|$ accurately. Therefore, this set of paths plays the role of the set of blue paths previously dicussed and they were used to calculate $\Delta T^{\ddagger}$, $\overline{T}^{\ddagger}$ and $\Delta E^{\ddagger}_{v}$ from Eqs. (61)-(64). We found $\Delta E^{\ddagger}_{v}\Delta T^{\ddagger} = 0.7\hbar$. Moreover, $\overline{T}^{\ddagger}$ is equal to 460 vibrational periods, which is a very long time. This is not surprizing since $T_k = (l_0+k)\pi/\omega^{\ddagger}$ and k ranges from 466 to $+\infty$. Note that resonant paths sojourn a very long time in the vicinity of the PO where the bending motion is much faster than the motion along the reaction coordinate. Therefore, the activated complex evolves adiabatically along the resonant paths. From the k-dependence of T_k and the fact that $k \geq 466$, the range of values of T_k is infinitely broad, thus explaining why the value of $\Delta T^{\ddagger}$ is also very large (520 vibrational periods). Conversely, $\Delta E^{\ddagger}_{v}$ is very small compared to $E^{\ddagger}_{zpe}$ (~ 3 cm^{-1} against 705 cm^{-1}). Therefore, we can say that the vibrational energy of the activated complex is "strictly" quantized right at the threshold, which is consistent with the fact that the activated complex evolves adiabatically for a very long time. If one increases the energy, the resonant paths no longer contribute to $S_{00}(E)$. The relevant paths are those defined by the values of k around the one that makes the phase $\Psi_k/\hbar$ minimal (see the blue squares in Fig. 17 for $E/E^{\ddagger}_{zpe} = 1.2$). It is a simple matter of algebra to show from Eq. (43) that $\frac{d^2\Psi_k}{dk^2}$ varies like $(E - E^{\ddagger}_{zpe})^{3/2}$ at the minimum of Ψ_k (see Fig. 17). Therefore, the larger the difference $E - E^{\ddagger}_{zpe}$, the narrower the range of k-values in which $exp\left(i\frac{\Psi_k}{\hbar}\right)$ does not oscillate too fast (these values define the blue paths). Since T_k is proportional to k, the width of the interval of T_k values decreases with $E - E^{\ddagger}_{zpe}$, thus implying that $\Delta T^{\ddagger}$ also decreases. Concomitantly, $\Delta E^{\ddagger}_{v}$ increases (see Fig. 20) in such a way that the vibrational energy of the activated complex is less and less quantized. At $E = 1.2E^{\ddagger}_{zpe}$, however, E_v is still roughly quantized since the uncertainty on the latter (~ 400 cm^{-1}) keeps reasonably small compared to the bending vibrational quantum (1410 cm^{-1}).

Below the threshold energy, y is assigned the statistical weight $p(y)$, defined as the squared modulus of the integrand of Eq. (57) mutliplied by a factor making the weight normalized to unity. The uncertainty $\Delta E^{\ddagger}_{v}$ on the vibrational energy [Eq. (58)] is then given by Eq. (61) with $\overline{E^{\ddagger n}_{v}} = \int_{-\infty}^{0} dy p(y) E^{\ddagger}_{v}(y)^n$, $n = 1, 2$. The uncertainty $\Delta T^{\ddagger}$ on the modulus of $T(y)$

[Eq. (59)] is given by similar expressions where the vibrational energy is replaced by $|T(y)|$. The findings are in line with those obtained previously. The product $\Delta E_v^\ddagger \Delta T^\ddagger$ is indeed equal to 0.60, 0.64 and 0.75 at $E/E_{zpe}^\ddagger = 0.95, 0.97$ and 0.99, respectively ($|S_{00}(E)|$ is negligible below $E/E_{zpe}^\ddagger = 0.95$, as can be seen in the upper panel of Fig. 6). Moreover, $\overline{E_v^\ddagger}$ is very close to $E_{zpe}^\ddagger$. Finally, the variations of $\Delta T^\ddagger$, $\overline{T}^\ddagger$ and $\Delta E_v^\ddagger$ with $|E - E_{zpe}^\ddagger|$ are as in Fig. 20. Therefore, the closer E from $E_{zpe}^\ddagger$, the more quantized the vibrational motion of the activated complex. Note that at $E = 0.95 E_{zpe}^\ddagger$, $\Delta E_v^\ddagger$ remains low compared to the bending vibrational quantum (205 cm^{-1} against 1410 cm^{-1}), so that the activated complex vibrational energy is still nearly quantized. It clearly appears from the results of Secs. 4.2.3 and 4.2.4 that real and pure imaginary times play a symmetric role depending on whether the energy is above or below the adiabatic barrier top.[6]

5 Conclusion

We have built a two-dimensional model of chemical reaction taking place in the electronic ground state, involving a single transition state (TS), and accounting for the correlation between the rotational motions of the separated reagents or products and the bending vibrational motion at the TS. This model process involves vibrationally nonadiabatic dynamics across the interaction region. Nevertheless, there is a region encompassing the TS in which the dynamics are vibrationally adiabatic (as it always is),[33] and we have called *activated complex* the molecular system orthogonal to the reaction path in the previous region. As is well known, the TS is intimately related to the existence of a periodic orbit (PO) located within the interaction region.[35,36]

For such a process occurring at low temperature, the two quantum mechanical effects known to play a key role within the interaction region are the zero point energy (ZPE) constraint at the TS, and tunneling through classically prohibited area.[9,12] Since in the general case, these two effects are likely to be entangled, we have decided not to include a

potential energy barrier in our model reaction so as to minimize the influence of tunneling on the dynamics. Therefore, we could focus our developments on the role played by the TS-ZPE in the dynamics, often empirically or pragmatically approached in the literature. The TS-ZPE has been denoted by $E^{\ddagger}_{zpe}$.

We have performed quantum scattering calculations showing that the energy threshold of the reaction is equal to $E^{\ddagger}_{zpe}$, as previously observed.[7–13] Therefore, the threshold is found to be the same as if the motion orthogonal to the reaction path were to evolve adiabatically. Schatz related this finding with the uncertainty principle.[9] Our goal was to describe and understand it in terms of classical paths within the framework of classical-limit quantum mechanics,[22,24,26,27] which assigns probability amplitudes to classical paths and make them interfere in accordance with the superposition principle. Two approaches have been used: the semiclassical initial value representation (SCIVR), more quantitative, with the hope of reproducing the threshold, and classical S-matrix theory (CSMT), more qualitative, in order to explain its origin. The conclusions of the study are as follows:

1) SCIVR reproduces very well the sigmoid shape of the quantum reaction probability. The threshold constraint on bending is thus properly built into semiclassical mechanics. CSMT shows that below $E^{\ddagger}_{zpe}$, reactive paths interfere destructively while a number of non-reactive paths whose phases are close to a stationary value interfere constructively. This inhibits the reactivity observed classical mechanically. Right at $E^{\ddagger}_{zpe}$, however, infinitely many reactive paths temporarily trapped in a metastable state at the TS – the resonant paths – interfere constructively, and the same thing happens for nonreactive trajectories. This resonant phase-matching enhances the reactivity. Above $E^{\ddagger}_{zpe}$, the opposite scenario to that below $E^{\ddagger}_{zpe}$ occurs, i.e., a number of reactive paths interfere constructively while non-reactive paths interfere destructively. As a result, the reactivity continues to rise to finally reach a plateau.

2) The reason why a quantum resonance occurs precisely at $E^{\ddagger}_{zpe}$ is the following: the relevant part of the phase of resonant paths is proportional to $[A(E) - \pi]$ where $A(E)$ is

the average vibrational action within the interaction region in $\hbar$ unit at the energy E. Since the resonant paths spend most of their long stay in the interaction region in the immediate vicinity of the PO underlying the TS, $A(E)$ is, to a good approximation, the vibrational action $A^{\ddagger}(E)$ corresponding to one vibrational period along the PO. $E^{\ddagger}_{zpe}$ turns out to be the value of E making $A^{\ddagger}(E)$ equal to π; the phases of resonant paths are then all equal and interfere constructively, thus explaining the quantum resonance. The equation $A^{\ddagger}(E) = \pi$ is nothing but the Bohr-Sommerfeld quantization rule applied to the activated complex.

3) Within the energy range considered in our study, the classical paths that primarily contribute to the semiclassical reactivity traverse the TS with a vibrational energy $E^{\ddagger}_{v}$ distributed around $E^{\ddagger}_{zpe}$, and an average value of $E^{\ddagger}_{v}$ nearly equal to $E^{\ddagger}_{zpe}$. Moreover, the standard deviation of $E^{\ddagger}_{v}$ multiplied by the standard deviation of the lifetime of the activated complex is equal to $\sim \hbar$. These findings support the idea that the activated complex is in a time-dependent quantum state satisfying the time-energy uncertainty principle.[13,56] Right at the threshold, however, the uncertainty on the lifetime of the activated complex is so large that its vibrational energy can be considered as quantized.

To summarize, we hope to have clearly highlighted from the properties of some relevant classical trajectories, in particular the periodic orbit underlying the transition state, the close link existing between the notions of reaction threshold, resonant trajectories, stationary phase, quantum resonance, and quantized activated complex or transition state.

Acknowledgements

LB is grateful to Pascal Larregaray and Matthew Braustein for stimulating discussions on the content of this paper and related topics.

Appendix A: Symmetry-adapted expression of $S_{j_2 j_1}(E)$

It is clear from Eq. (12) that if $J_1 = j_1 = 0$, $\overline{\phi}_1 = \phi_1$. Eq. (14) can thus be rewritten as:

$$S_{j_2 0}(E) = \frac{1}{2\pi} \int_0^{\pi} d\phi_1 [f(-\phi_1) + f(\phi_1)] \tag{A.1}$$

with

$$f(\phi_1) = \left| \frac{\partial \overline{\phi}_2}{\partial \phi_1} \bigg|_{j_1} \right|^{1/2} e^{i(\Phi - \pi\bar{\nu}/2)} \rho(\phi_1). \tag{A.2}$$

Moreover, the PES is symmetric with respect to the R-axis (see Fig. 1). Therefore, the trajectory starting from ϕ_1 (see the yellow path in Fig. 1), will be the symmetric with respect to the R-axis of the trajectory starting from $-\phi_1$. Consequently, $\phi(\phi_1, \tau) = -\phi(-\phi_1, \tau)$, $J(\phi_1, \tau) = -J(-\phi_1, \tau)$, $R(\phi_1, \tau) = R(-\phi_1, \tau)$, $P(\phi_1, \tau) = P(-\phi_1, \tau)$, $\overline{\phi}_2(\phi_1) = -\overline{\phi}_2(-\phi_1)$ (see Eq. (13)), $\Omega(\phi_1) = \Omega(-\phi_1)$, $\bar{\nu}(\phi_1) = \bar{\nu}(-\phi_1)$ and $\rho(\phi_1) = \rho(-\phi_1)$. Hence, it is a simple matter of algebra to check from Eq. (15) that

$$\Phi(-\phi_1) = \Phi(\phi_1) + 2j_2 \overline{\phi}_2(\phi_1). \tag{A.3}$$

Overall, we finally have

$$S_{j_2 0}(E) = \frac{1}{2\pi} \int_0^{\pi} d\phi_1 \left| \frac{\partial \overline{\phi}_2}{\partial \phi_1} \bigg|_{j_1} \right|^{1/2} e^{i(\Phi - \pi\bar{\nu}/2)} \left[1 + e^{i2j_2 \overline{\phi}_2}\right] \rho(\phi_1). \tag{A.4}$$

This expression allowed us to run twice less trajectories for the same accuracy compared to Eq. (14).

Appendix B: Approximation of the prefactors in Eq. (21)

We have seen in Sec. 4.1.4 that $|S_{00}(E)|^2$ and $|S'_{00}(E)|^2$ do not diverge at the threshold because the prefactors in Eq. (21) are approximately proportional to $1/k^{3/2}$. We now prove

this assertion. A few mathematical steps involving Eq. (32) with $\tau = T$, and Eqs. (29), (33) and (38), lead to

$$\left|\frac{\partial J_2}{\partial \overline{\phi}_1}\Big|_k\right| = \frac{2I\pi^3(l_0+k)^3}{\mu\omega^{\ddagger 2}\Delta^2}\left[E - \frac{\mu\omega^{\ddagger 2}\Delta^2}{2\pi^2(l_0+k)^2}\right]^{1/2}. \tag{B.1}$$

At the threshold, those paths mostly contributing to the sum in Eq. (21) are the resonant paths for which k is much larger than l_0, so $l_0 + k$ can be replaced by k in Eq. (B.1). Thus, its right-hand-side is proportional to k^3, and the prefactors in Eq. (21) to $1/k^{3/2}$.

Appendix C: SCIVR Folding functions

Within the SCIVR approach, the way in which S-matrix elements are built from the amplitudes assigned to the trajectories can be qualitatively understood as follows. Based on Eq. (14), we define the *folding F function* associated with $S_{00}(E)$ by

$$F(\overline{\phi}_{max}) = \frac{1}{2\pi}\int_{-\overline{\phi}_{max}}^{\overline{\phi}_{max}} d\overline{\phi}_1 \left|\frac{\partial \overline{\phi}_2}{\partial \overline{\phi}_1}\Big|_{j_1=0}\right|^{1/2} e^{i(\Phi - \pi\bar{\nu}/2)}. \tag{C.1}$$

If we take $\overline{\phi}_{max}$ at $\overline{\phi}_{po}$, the integral in Eq. (C.1) is over the whole set of reactive trajectories (see Fig. 3; since $j_1 = 0$, J_2 is an odd function of $\overline{\phi}_1$, and trajectories are reactive from $\overline{\phi}_1 = -\overline{\phi}_{po}$ to $\overline{\phi}_1 = \overline{\phi}_{po}$). Therefore, $F(\overline{\phi}_{po}) = S_{00}(E)$ [see Eq. (14)]. We consider the path followed by $F(\overline{\phi}_{max})$ in the complex plane when $\overline{\phi}_{max}$ increases from 0 to $\overline{\phi}_{po}$ [$F(\overline{\phi}_{max})$ is simply denoted by F]. This path is represented at the three energies $0.8E^{\ddagger}_{zpe}$, $E^{\ddagger}_{zpe}$ and $1.2E^{\ddagger}_{zpe}$ by the blue curves in Fig. 21. They all start from the origin of the complex plane. The folding F' function associated with $S'_{00}(E)$ is defined by

$$F'(\overline{\phi}_{max}) = \frac{1}{2\pi}\int_{\pi-\overline{\phi}_{max}}^{\pi+\overline{\phi}_{max}} d\overline{\phi}_1 \left|\frac{\partial \overline{\phi}_2}{\partial \overline{\phi}_1}\Big|_{j_1=0}\right|^{1/2} e^{i(\Phi - \pi\bar{\nu}/2)}. \tag{C.2}$$

If we take $\overline{\phi}_{max}$ at $\pi - \overline{\phi}_{po}$, the integral in Eq. (C.2) is over the whole set of nonreactive trajectories (see Fig. 3; since $j_1 = 0$, J_2 is an odd function of $[\overline{\phi}_1 - \pi]$, and trajectories are

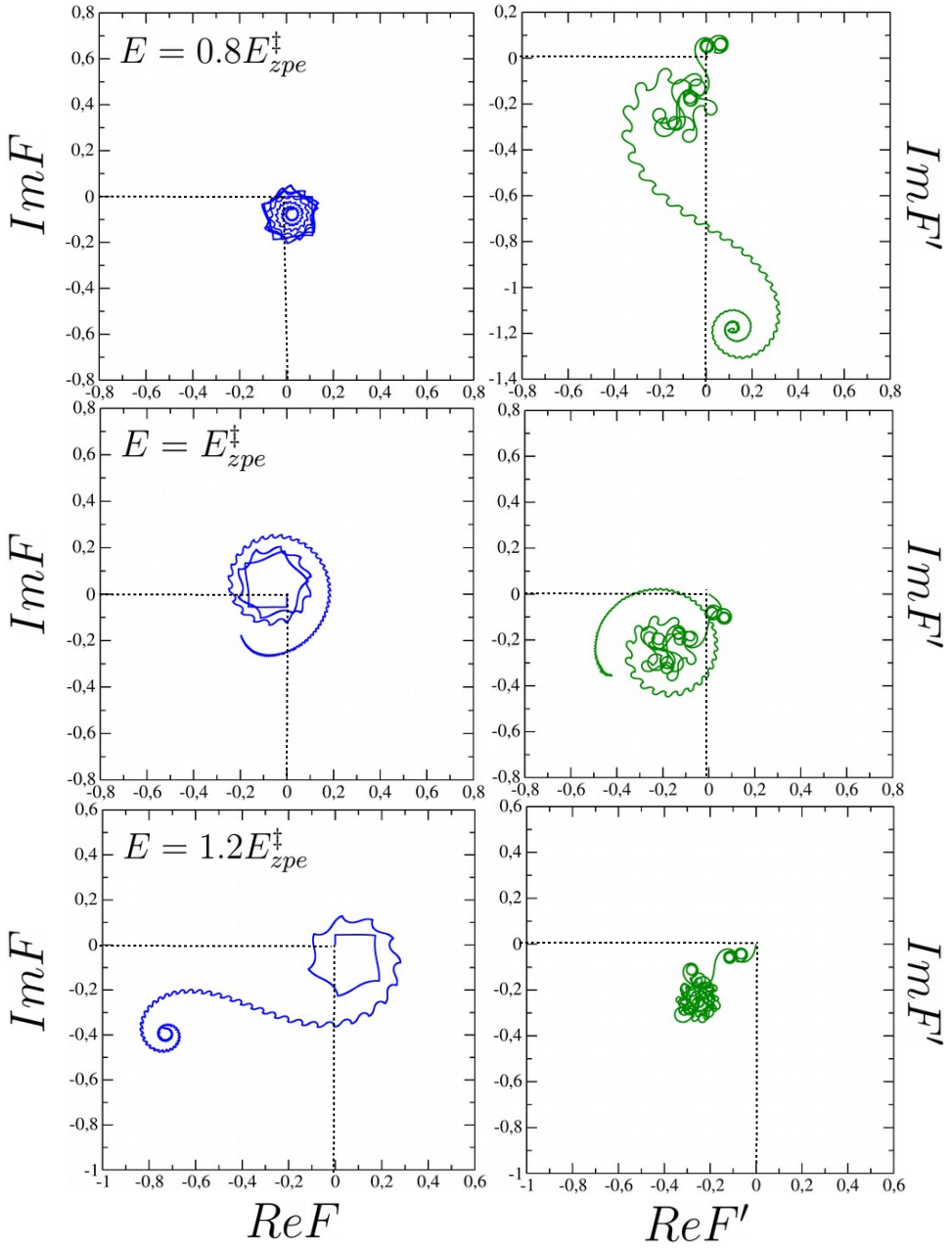

Figure 21: Representation in the complex plane of the SCIVR folding functions F and F', defined by Eq. (C.1). See text for more details.

reactive from $\overline{\phi}_1 = \overline{\phi}_{po}$ to $\overline{\phi}_1 = 2\pi - \overline{\phi}_{po}$). Thus, $F'(\pi - \overline{\phi}_{po}) = S'_{00}(E)$. The paths followed by $F'(\overline{\phi}_{max}) \equiv F'$ in the complex plane at $0.8E^{\ddagger}_{zpe}$, $E^{\ddagger}_{zpe}$ and $1.2E^{\ddagger}_{zpe}$ are shown by the green curves in Fig. 21. Apart from the zig-zags, or the initial loops, the curves in Fig. 21 closely

resemble those in Fig. 13. This is true across the entire green curves, and across a large part of the blue curves. The blue CSMT curves, however, do not start from the origin like the blue SCIVR curves for the following reason: CSMT does not work when $\frac{\partial J_2}{\partial \bar{\phi}_1}\big|_k$ takes very small value, as is the case for the reactive paths corresponding to $k \leq 2$ (see Fig. 3). The prefactor in Eq. (21) is indeed strongly overestimated for $k \leq 2$, and the initial variation of F is unrealistic. This is why we ignored the first three terms of the sum in Eq. (21) for the calculation of F. On the other hand, we took into account all the terms for the calculation of F' since the prefactor is never overestimated.

Data Availability Statements

The data that support the findings of this study are available from the corresponding authors upon reasonable request.

References

(1) Glasstone, S.; Laidler, K. J.; Eyring, H. *The theory of rate processes: the kinetics of chemical reactions, viscosity, diffusion and electrochemical phenomena*; McGraw-Hill, New York, 1941.

(2) Henriksen, N. E.; Hanssen, F. Y. *Theories of Molecular Reaction Dynamics*; Oxford University Press, 2008.

(3) Fernandez-Ramos, A.; Miller, J. A.; Klippenstein, S. J.; Truhlar, D. G. Modeling the kinetics of bimolecular reactions. *Chem. Rev.* **2006**, *106*, 4518.

(4) The threshold energy depends on the total angular momentum J. When the latter increases, so does the effective barrier height and, consequently, the threshold energy. Therefore, the threshold energy observed in a chemical reaction studied in a crossed

molecular beam experiment, where total J is not controlled, is the one corresponding to total J equal 0.

(5) Rosenstock, H. M. On the Classical Approximation in the Statistical Theory of Mass Spectra. *J. Chem. Phys.* **1961**, *34*, 2182.

(6) Pollak, E. The significance of imaginary time in quantal reactive scattering. *J. Chem. Phys.* **1985**, *83*, 1111.

(7) Truhlar, D. G.; Kuppermann, A. Exact and Approximate Quantum Mechanical Reaction Probabilities and Rate Constants for the Collinear H + H_2 Reaction. *J. Chem. Phys.* **1972**, *56*, 2232.

(8) Schatz, G. C.; Kuppermann, A. Quantum mechanical reactive scattering for three dimensional atom plus diatom systems. II. Accurate cross sections for H+H_2. *J. Chem. Phys.* **1976**, *65*, 4668.

(9) Schatz, G. The origin of cross section thresholds in H + H_2: Why quantum dynamics appears to be more vibrationally adiabatic than classical dynamics. *J. Chem. Phys.* **1983**, *79*, 5386.

(10) Pollak, E.; Wyatt, R. E. Adiabatic-sudden transition in chemical reactions: study of a model for H+H_2 ($v = 1$). *Chem. Phys. Lett.* **1984**, *110*, 340.

(11) Pollak, E. Harmonic tunneling corrections to sudden and adiabatic transition state theory. *J. Chem. Phys.* **1985**, *82*, 106.

(12) Schatz, G. C. Tunneling in bimolecular reactions. *Chem. Rev.* **1987**, *87*, 81.

(13) Chatfield, D. C.; Friedman, R. S.; Truhlar, D. G.; Garrett, B. C.; Schwenke, D. W. Global control of suprathreshold reactivity by quantized transition states. *J. Am. Chem. Soc.* **1991**, *113*, 486.

(14) Garashchuk, S.; Light, J. C. Semiclassical application of the Møller operators in reactive scattering. *J. Chem. Phys.* **2001**, *114*, 1060.

(15) Quack, M.; Troe, J. Specific Rate Constants of Unimolecular Processes II. Adiabatic Channel Model. *Ber. Bunsen. Phys. Chem.* **1974**, *78*, 240.

(16) Walker, R. B.; Hayes, E. F. Theoretical Analysis of the Quantum Contributions to the Reactions $H_2(v{=}1) + H \rightarrow H + H_2(v'{=}0,1)$ and $H_2(v{=}1) + D \rightarrow H + HD_2(v'{=}0,1)$. *J. Phys. Chem.* **1983**, *87*, 1255.

(17) Bowman, J. M.; Ju, G.-Z.; Lee, K. T. New approximate quantum cross sections for the $H + H_2$ reaction. *J. Chem. Phys.* **1981**, *75*, 5199.

(18) Stoecklin, T.; Dateo, C. E.; Clary, D. C. Rate constant calculations on fast diatomdiatom reactions. *J. Chem. Soc., Faraday Trans.* **1991**, *87*, 1667.

(19) Konings, M.; Desrousseaux, B.; Lique, F.; Loreau, J. Benchmarking an improved statistical adiabatic channel model for competing inelastic and reactive processes. *J. Chem. Phys.* **2021**, *155*, 104302.

(20) Abu-Salbi, N.; Kouri, D. J.; Baer, M.; Pollak, E. A study of the quantal time delay matrix in collinear reactive scattering. *J. Chem. Phys.* **1985**, *82*, 4500.

(21) Miller, W. H. Semiclassical Theory of Atom-Diatom Collisions: Path Integrals and the Classical S Matrix. *J. Chem. Phys.* **1970**, *53*, 1949.

(22) Miller, W. H. Classical S Matrix: Numerical Application to Inelastic Collisions. *J. Chem. Phys.* **1970**, *53*, 3578.

(23) Miller, W. H. Classical-limit quantum mechanics and the theory of molecular collisions. *Adv. Chem. Phys.* **1974**, *25*, 69.

(24) Marcus, R. A. Extension of the WKB method to wave functions and transition probability amplitudes (S-matrix) for inelastic or reactive collisions. *Chem. Phys. Lett.* **1970**, *7*, 525.

(25) Stine, J. R.; Marcus, R. A. Semiclassical S matrix theory for a compound state resonance in the reactive collinear H + H_2 collision. *Chem. Phys. Lett* **1974**, *29*, 575.

(26) Miller, W. H. The semiclassical initial value representation: A potentially practical way for adding quantum effects to classical molecular dynamics simulations. *J. Phys. Chem. A* **2001**, *105*, 2942.

(27) Bonnet, L. Semiclassical initial value theory of rotationally inelastic scattering: Some remarks on the phase index in the interaction picture. *J. Chem. Phys.* **2018**, *148*, 194104.

(28) Bonnet, L.; Crespos, C. Phase-index problem in the semiclassical description of molecular collisions. *Phys. Rev. A* **2008**, *78*, 062713.

(29) Miller, W. H. The Classical S-Matrix in Molecular Collisions. *Adv. Chem. Phys.* **1975**, *30*, 77.

(30) Goldfarb, Y.; Schiff, J.; Tannor, D. J. Complex trajectory method in time-dependent WKB. *J. Chem. Phys.* **2008**, *128*, 164114.

(31) CSMT and the SCIVR approach used in this work involve in their derivations a time-energy Fourier transform that is analytically performed within the stationary phase approximation (SPA).[22,23] This implies that the trajectories contributing to S-matrix elements must be run at the energy for which one wishes to obtain these elements. Therefore, these trajectories are exactly the same as those involved in Gaussian binning[28] or standard QCT calculations[3] and thus do not allow for tunneling. In order to make them tunnel through configuration space regions that are classically prohibited

either dynamically or energetically, one must deform the time path from the real axis to the complex plane, as clearly shown in Ref.[29]. Note that tunneling is partly taken into account from real-time paths if the time-energy Fourier transform is performed numerically, instead of analytically by the SPA.

(32) Friedman, R. S.; Truhlar, D. G. Chemical reaction thresholds are resonances. *Chem. Phys. Lett.* **1991**, *183*, 539.

(33) Pollak, E. *Periodic Orbits and Reactive Scattering: Past, Present and Future. In: Clary, D.C. (eds) The Theory of Chemical Reaction Dynamics. NATO ASI Series, vol 170.*; Springer, Dordrecht, 1986.

(34) Gustafsson, M.; Skodje, R. T. The state-to-state-to-state model for direct chemical reactions: Application to D+H_2 $\rightarrow$ HD+H. *J. Chem. Phys.* **2006**, *124*, 144311.

(35) Pechukas, P.; Pollak, E. Transition states, trapped trajectories, and classical bound states embedded in the continuum. *J. Chem. Phys.* **1978**, *69*, 1218.

(36) Pechukas, P.; Pollak, E. Classical transition state theory is exact if the transition state is unique. *J. Chem. Phys.* **1979**, *71*, 2062.

(37) Tannor, D. J. *Introduction to quantum mechanics. A time-dependent perspective*; University Science Books, 2007.

(38) Feit, M.; Fleck, J.; Steiger, A. Solution of the Schrödinger equation by a spectral method. *Journal of Computational Physics* **1982**, *47*, 412–433.

(39) Feit, M. D.; Fleck, J. A. Solution of the Schrdinger equation by a spectral method II: Vibrational energy levels of triatomic molecules. *The Journal of Chemical Physics* **1983**, *78*, 301–308.

(40) Light, J. C.; Hamilton, I. P.; Lill, J. V. Generalized discrete variable approximation in quantum mechanics. *The Journal of Chemical Physics* **1985**, *82*, 1400–1409.

(41) Lill, J. V.; Parker, G. A.; Light, J. C. The discrete variable finite basis approach to quantum scattering. *The Journal of Chemical Physics* **1986**, *85*, 900–910.

(42) Kosloff, R. Time-Dependent Quantum-Mechanical Methods for Molecular Dynamics. *Journal of Physical Chemistry* **1988**, *92*, 2087–2100.

(43) Kosloff, D.; Kosloff, R. A fourier method solution for the time dependent Schrödinger equation as a tool in molecular dynamics. *Journal of Computational Physics* **1983**, *52*, 35 – 53.

(44) Riss, U. V.; Meyer, H.-D. The transformative complex absorbing potential method: a bridge between complex absorbing potentials and smooth exterior scaling. *J. Phys. B: At., Mol. Opt. Phys.* **1998**, *31*, 2279.

(45) Porter, R.; Raff, L. M. In *Introduction to quantum mechanics. A time-dependent perspective*; Miller, W. H., Ed.; Dynamics of Molecular Collisions; Plenum, New York, 1976.

(46) Sewell, T.; Thomson, D. Classical Trajectory Methods for Polyatomic Molecules. *Int. J. Mod. Phys. B* **1997**, *11*, 1067.

(47) William, H.; Teukolsky, S. A.; Vetterling, W. T.; Flannery, B. P. *Numerical Recipes: The Art of Scientific Computing, 3rd ed.*; Cambridge University Press, New York, 2007.

(48) Bonnet, L. Semiclassical initial value representation: From Møller to Miller. *J. Chem. Phys.* **2020**, *153*, 174102.

(49) Bonnet, L. Semiclassical descriptions of rotational transitions in natural and shifted angles: Analysis of unexpected results. *J. Chem. Phys.* **2021**, *155*, 174103.

(50) Bonnet, L.; Rayez, J. C. Gaussian weighting in the quasiclassical trajectory method. *Chem. Phys. Lett.* **2004**, *397*, 106–109.

(51) Gutzwiller, M. C. *Chaos in Classical and Quantum Mechanics*; Springer-Verlag, New York, 1990.

(52) Stockmann, H.-J. *Quantum Chaos. An Introduction*; Cambridge University Press, New York, 1999.

(53) The fact that the phase decreases monotonically within the ranges $\sim [0, \pi/5]$ and $\sim [\pi/2, \pi]$ is a necessary condition for the existence of stationary phases. Indeed, if the phase was flat within these ranges, adding a peak to it, either down or up, would not make any phase stationary.

(54) Pollak, E.; Child, M. A simple classical prediction of quantal resonances in collinear reactive scattering. *Chem. Phys.* **1981**, *60*, 23.

(55) Few studies of chemical reaction resonances performed within the semiclassical theory of molecular collisions are available in the literature. A pioneering study dealing with a resonance above threshold in the collinear reaction H + H_2 is that of Stine and Marcus.[25].

(56) Dai, D.; Wang, C. C.; Harich, S. A.; Wang, X.; Yang, X.; Chao, S. D.; Skodje, R. T. Interference of Quantized Transition-State Pathways in the H + $D_2 \longrightarrow$ D + HD Chemical Reaction. *Science* **2003**, *300*, 1730.

(57) Weber, H. J.; Arfken, G. B. *Essential Mathematical Methods for Physicists*; Academic Press, 2003.

(58) It is quite disconcerting to find oneself manipulating complex times when one has done everything to avoid them. We have indeed assumed that there is no potential energy barrier along the reaction path in order to be able to describe the dynamics with good accuracy using only real time trajectories. However, it is the asymptotic approximation on which the saddle point is based, namely that $\hbar$ is infinitely small, which makes

imaginary times appear in the developments. This is clearly explained by Miller in Sec. IV.A of Ref.[29]. The nice thing here is that the modulous of these times is shown in Sec. 4.2.4 to satisfy the time-energy uncertainty principle.